

A GROUND BASED OPTICAL SURVEY FOR GPS SOLAR PANEL ARCING

by

Shane Walsh

Copyright © Shane Walsh 2019

A Thesis Submitted to the Faculty of the

JAMES C. WYANT COLLEGE OF OPTICAL SCIENCES

In Partial Fulfillment of the Requirements

For the Degree of

MASTER OF SCIENCE

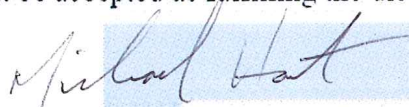
In the Graduate College

THE UNIVERSITY OF ARIZONA

2019

THE UNIVERSITY OF ARIZONA
GRADUATE COLLEGE

As members of the Master's Committee, we certify that we have read the thesis prepared by Shane Walsh, titled A Ground Based Optical Survey for GPS Solar Panel Arcing and recommend that it be accepted as fulfilling the dissertation requirement for the Master's Degree.



Michael Hart

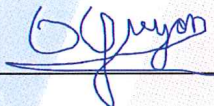
Date: May 9, 2019



Eric Pearce

Digitally signed by Eric C. Pearce
Date: 2019.05.07 11:57:32
-07'00'

Date: May 7, 2019

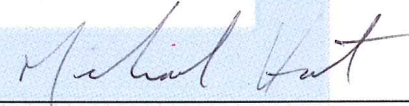


Olivier Guyon

Date: May 6, 2019

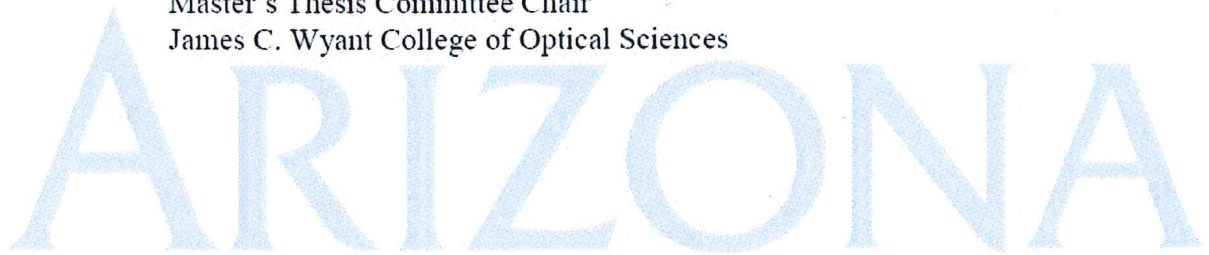
Final approval and acceptance of this thesis is contingent upon the candidate's submission of the final copies of the thesis to the Graduate College.

I hereby certify that I have read this thesis prepared under my direction and recommend that it be accepted as fulfilling the Master's requirement.



Michael Hart
Master's Thesis Committee Chair
James C. Wyant College of Optical Sciences

Date: May 9, 2019



Acknowledgements

Thanks to my Master's committee Michael Hart, Eric Pearce, and Olivier Guyon for serving on my committee and assistance with planning and observations, Harry Krantz for assistance with the EMCCD, Will Goble and Ben Weiner for making observations run so smoothly, Grant Williams for the generous allocation of MMT Director's time, and Richard Rast for facilitating the project and his boundless encouragement.

I'd also like to thank my LBTO superiors, notably Michelle Edwards, for the flexibility and support allowing me to undertake this program during these three years.

Finally, thanks to my wife Valentina and son Satchel for their patience during these busy times. It's almost over!

Dedication

To Satchel, I hope your curiosity and wonder never wane.

Contents

| | |
|--|-----------|
| List of Figures | 7 |
| List of Tables | 10 |
| Abstract | 11 |
| 1 Introduction | 12 |
| 1.1 The GPS Power Degradation Anomaly | 12 |
| 1.2 Radiation Damage | 12 |
| 1.3 Contamination | 14 |
| 1.4 Arc Induced Contamination | 15 |
| 1.5 Expected Signal | 16 |
| 2 Observing Strategy | 17 |
| 2.1 The MMT and Red Channel Spectrograph | 17 |
| 2.2 EMCCD Detector | 18 |
| 2.3 The Optomechanics | 19 |
| 2.4 Benchtest | 21 |
| 2.4.1 Relay Lens Quality | 21 |
| 2.4.2 Detector Quality | 24 |
| 3 Results | 28 |
| 3.1 Data Acquisition | 28 |
| 3.2 Data Processing | 31 |
| 3.3 Sensitivity | 31 |
| 3.4 Detection Algorithm | 34 |
| 3.5 Monte Carlo Simulation | 35 |
| 3.6 Results | 40 |
| 3.6.1 NAVSTAR 48 | 40 |
| 3.6.2 NAVSTAR 59 | 46 |
| 3.6.3 NAVSTAR 65 | 47 |

| | |
|---|-----------|
| 4 Conclusion | 49 |
| 4.1 Future Work | 49 |
| A Candidate detections | 51 |
| A.1 NAVSTAR 48, 4.7σ Threshold | 51 |
| B Mounting Bracket Engineering Drawings | 59 |
| C MATLAB Code | 63 |
| C.1 spade_search.m | 63 |
| C.2 spade_monte.m | 66 |
| C.3 arcmaker.m | 68 |
| Bibliography | 69 |

List of Figures

| | | |
|-----|--|----|
| 1.1 | Power degradation of NAVSTAR 4 compared with radiation only and radiation plus contamination models. (Marvin et al., 1988). | 13 |
| 1.2 | Actual solar cell current vs time for NAVSTAR 49, compared with expected degradation from measured radiation (JPL and NRL models), and with purely modelled degradation (AE8MAX) (Messenger et al., 2011). | 14 |
| 2.1 | The MMT at Mt Hopkins, Arizona. Image courtesy of MMTO. | 18 |
| 2.2 | Schematic of the Red Channel camera. (Schmidt et al., 1989) | 19 |
| 2.3 | Mounting surface of the Red Channel dewar. Image courtesy of Will Goble, MMTO. | 20 |
| 2.4 | Mockup of EMCCD interfaced with Red Channel. | 21 |
| 2.5 | The completed bracket, fabricated in the Steward Observatory machine shop. | 22 |
| 2.6 | <i>Top:</i> Focused image of $10\mu\text{m}$ pinhole. <i>Bottom:</i> PSF profiles in x and y direction. The FWHM is ~ 2 pixels, or $32\mu\text{m}$ | 23 |
| 2.7 | Imaging target simulating plate scale of MMT Red Channel detector. The 2 arcminute box is $8\text{ mm} \times 8\text{ mm}$ | 24 |
| 2.8 | Imaging target imaged through relay lens with 1×1 binning (top) and 2×2 binning (bottom). The outer edge of the outermost square is 2 arcminutes. | 25 |
| 2.9 | Signal to Noise Ratio as a function of arc counts and EM gain, assuming sky count rate of 6695 ph/s/pixel , readout of noise of $67e^-$, 8 ms exposure, excess noise factor $F=1.4$, and signal measurement over 5×5 pixel area. | 27 |
| 3.1 | The EMCCD mounted to the Red Channel. | 29 |
| 3.2 | Number of photons/s/ \AA mm^2 vs wavelength for Hz 14 spectrum. Dashed line is from Massey et al. (1988), solid line includes relay lens transmission and EMCCD quantum efficiency losses. | 32 |

| | | |
|------|--|----|
| 3.3 | Relay lens transmission and EMCCD quantum efficiency versus wavelength. | 33 |
| 3.4 | Raw image of Hz 14. Green box shows pixels used to calculate total star counts, red box shows pixels used to calculate sky counts. These calculations were done on the flat-fielded images. | 34 |
| 3.5 | Detection algorithm flow. Five images are smoothed, median combined, and stars masked out. The mask is applied to the individual smoothed images, leaving only objects present in a single image to remain as a significant detection. | 36 |
| 3.6 | Simulated arcs for various numbers of photons. | 37 |
| 3.7 | Detection significance versus arc photon count. The solid lines show the mean values for arcs (red) and background (blue). The dashed lines are ± 3 standard deviations for arc detections (not the same as σ on the y-scale) and $+4.5$ standard deviations for the background. | 38 |
| 3.8 | Fraction of simulated arcs detected versus arc photon count. | 39 |
| 3.9 | The interpolated path of NAVSTAR 48 during the observation period (green line) and the offset field searched for false positives (red box). The bright object at the start of the green line is NAVSTAR 49 before eclipse. | 41 |
| 3.10 | False positive detected away from satellite. Green circle is the blank area searched. | 41 |
| 3.11 | Image prior to detection, image of detection, image after detection, and stacked, smoothed image centered on detection. <i>Top:</i> In this case, the detection is a cosmic ray, but the background stars are clearly visible in the stacked image while invisible in the individual images. <i>Bottom:</i> Detection from image #287817 showing that the satellite is present in most or all 51 images, therefore is not an arc but rather the partially illuminated satellite exiting eclipse. | 42 |
| 3.12 | <i>Top:</i> Persistence caused by bright star (Taken from NAVSTAR 65 dataset). <i>Bottom:</i> Possible NAVSTAR 48 false detection caused by persistence. | 43 |
| 3.13 | Detection significance versus image number for Arecibo candidate times. The red line indicates the nominal detection threshold of 4.7σ | 45 |
| 3.14 | <i>Top:</i> Smoothed image of frame with fluctuation above threshold, corresponding to Arecibo detection at 5:06:19 UTC. Green cross is expected satellite position. <i>Bottom:</i> Image prior to detection, image of detection, image after detection, and stacked, smoothed image centered on detection showing the presence of faint stars responsible for detection. Green circle is expected satellite position. | 46 |

-
- 3.15 Candidate detection for NAVSTAR 65. *Left:* Single bias-subtracted, flat-fielded image. *Center:* Smoothed single image. *Right:* 51 Stacked and smoothed frames. Green circle shows interpolated NAVSTAR 65 location. 48

List of Tables

| | | |
|-----|---|----|
| 2.1 | Measured readout noise for various modes. | 26 |
| 2.2 | Values used to estimate sky background. | 26 |
| 3.1 | Target information and eclipse times. | 28 |
| 3.2 | Candidate detections for NAVSTAR 48. | 44 |

Abstract

In an attempt to confirm electrostatic discharge induced contamination as responsible for the excess power loss of GPS solar arrays, three GPS satellites were observed at the MMT using a sensitive Electron Multiplying CCD (EMCCD) with the aim of catching the microsecond optical emission of solar panel arcing. One of these satellites (NAVSTAR 48) was concurrently observed with the Arecibo radio telescope in the hopes that coincident optical and radio detections would all but confirm the hypothesis. Unfortunately, owing to $\sim 75\%$ transmission losses, optical arc detections could not be conclusively confirmed or ruled out. Detections above the nominal threshold were present more frequently than expected from random fluctuations, but the lack of coincidence with Arecibo detections and the similar number of detections away from the satellite imply a cause other than arcs, most likely non-Gaussian noise behavior. One of the other satellites, NAVSTAR 65, yielded a promising candidate with a brightness consistent with a fully discharging arc of a Block II-F solar array. However, without external confirmation from satellite telemetry, the detection significance is not sufficient to unambiguously label this event as an arc. If the observations could be repeated with transmission losses of 30% or less, the 50% detection efficiency of arcs would improve from 200-photon arcs to 70-photons or better. This would make the difference between being sensitive to *some* full discharge arcs or *most* partial discharge arcs, although requiring substantial redesign of the observing strategy.

Chapter 1

Introduction

Confused, would we?

–Homer Simpson

1.1 The GPS Power Degradation Anomaly

With an energy flux of 1370 W/m^2 at 1 AU, solar power is the logical source of operational power for spacecraft in the inner solar system. Photovoltaics (PV), whether for use on Earth or in space, show performance degradation over time. Terrestrial PV modules typically show $< 1\%$ per year (C. Jordan & R. Kurtz, 2013) due to climatic effects of thermal cycling, moisture intrusion, etc. Panels in space are not subject to the same level of thermal cycling or effects of humidity as those on the ground, but in the Medium Earth Orbit (MEO) domain of GPS satellites, they must contend with the radiation and plasma environments conspiring to degrade performance. Despite best efforts to engineer satellites to handle the space environment, the measured power output of GPS solar arrays degrades faster than expected. In order to maintain sufficient power, the panels must be oversized by $\sim 25\%$, adding significantly to launch weight and cost. If the cause of the excess power loss could be identified and a solution engineered, the reduction in spacecraft size would be sufficient to allow two GPS satellites to be launched in a single launch vehicle (R. Rast, personal communication, Jan 11, 2019).

1.2 Radiation Damage

The mechanism by which radiation damages solar arrays depends on the type of incident particle, and the magnitude of the effect depends on the type of array used. Silicon (Si) cells are cheap but offer little radiation resistance, while costlier Indium Phosphide (InP) cells offer higher efficiency and radiation resistance. Regardless of

the particulars, all cells will succumb to total radiation dose effects causing defects in the lattice structure, producing less power at the end of their life than the beginning. Shielding with a transparent coverslide provides some protection, but increasing the thickness of these coverslides adds costly weight and transmission loss, so some power loss to radiation is for all practical purposes, unavoidable.

The predicted degradation rate and end-of-life power production due to radiation is factored into the design of spacecraft PV modules, but Marvin et al. (1988) found that at after five and ten years of operation, the first generation Block I NAVSTAR 1-6 GPS spacecraft showed power losses of 23% and 37% respectively; a significant excess beyond the 18% and 21% expected at these epochs from radiation damage alone (Figure 1.1).

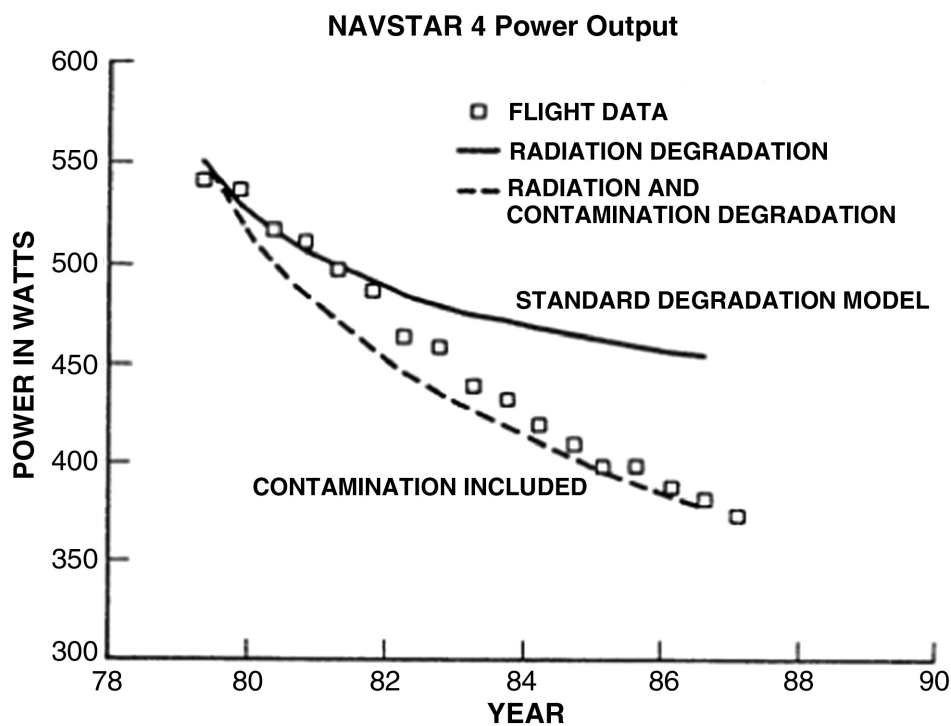


Fig. 1.1 — Power degradation of NAVSTAR 4 compared with radiation only and radiation plus contamination models. (Marvin et al., 1988).

The immediate question would be whether the radiation models are wrong. Messenger et al. (2011) used data from GPS satellite NAVSTAR 49, a Block IIR spacecraft carrying an onboard radiation dosimetry detector, to calculate the expected power degradation from actual radiation exposure. They used two different models to convert particle fluence to power degradation, both of which showed excellent agreement with each other and with the NASA AE8MAX electron environment model, but fell far short of agreement with actual power degradation (Figure 1.2). Hence, there is a source of degradation in addition to radiation.

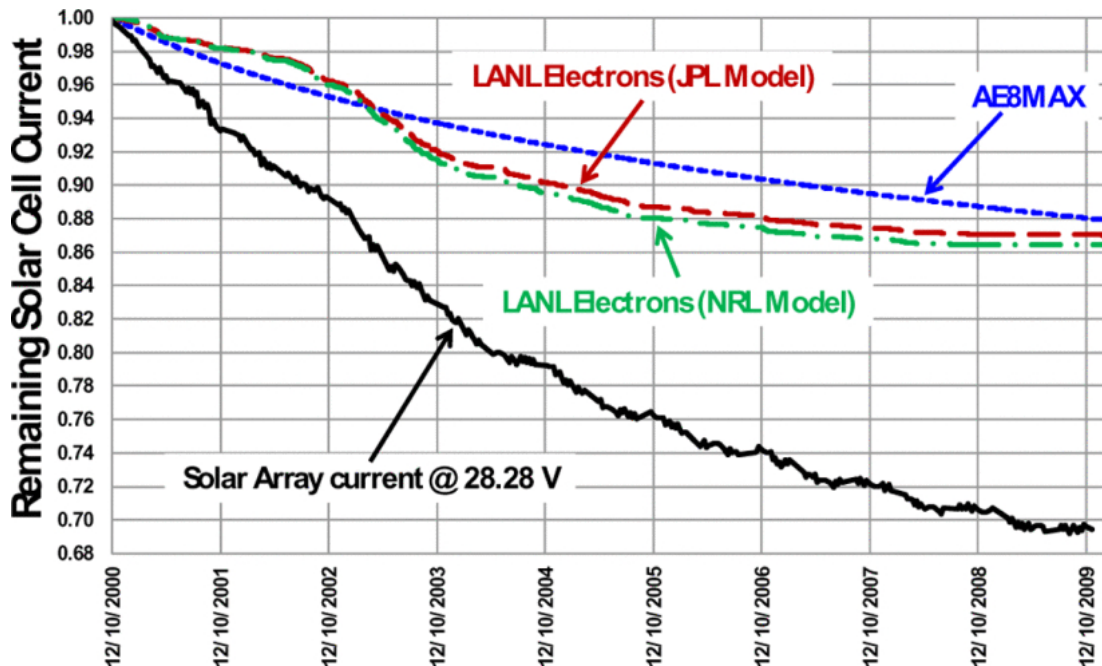


Fig. 1.2 — Actual solar cell current vs time for NAVSTAR 49, compared with expected degradation from measured radiation (JPL and NRL models), and with purely modelled degradation (AE8MAX) (Messenger et al., 2011).

1.3 Contamination

Spacecraft are subject to particulate and molecular contamination. Particulate contamination, from micron sized particles, is dependent upon the cleanliness of the ground facility in which it is constructed and as such, would not cause continual degradation over the multi-year lifespan of most spacecraft. Molecular contamination, from individual molecules, can occur when material outgasses from the spacecraft itself, being strongest after launch but can continue over time. The residence time of molecular contamination is a function of the temperature of the surface on which it finds itself; the higher the temperature, the more likely a thermal interaction will eject the molecule back into space. At a temperature of $\sim 60^{\circ}\text{C}$, solar panels were expected to be largely impervious due to very short residence times.

Photocontamination of the solar array surfaces, where outgassed material from other spacecraft components is deposited and then fixed by UV radiation, was present in early generations of GPS satellites and suspected as a cause of the excess degradation (Tribble & Haffner, 1991). Later GPS satellites were engineered to mitigate this effect by eliminating line of sight to sources of outgassing, albeit without a commensurate improvement in array performance (Ferguson et al., 2016). The degradation rate is consistent with radiation damage plus contamination (as opposed to component failures which would produce abrupt instead of gradual changes in power generation), although

the source of the contamination has not been conclusively identified.

1.4 Arc Induced Contamination

One proposed mechanism, and the subject of this work, is electrostatic arc-induced contamination first put forward by Ferguson et al. (2016). As satellites orbit through the plasma of space, they can build a potential of thousands of volts between themselves and the environment, as well as between satellite components. When this potential reaches a threshold, it leads to an electrostatic discharge.

The solar arrays of spacecraft, with their large surface area and direct exposure to space, are particularly susceptible to this. These discharges could cause contamination of the solar array surface, attenuating the incident sunlight and reducing power output. They can also cause more acute symptoms of electrical anomalies resulting in telemetry glitches, bit-flips, etc. but without external confirmation, arcing cannot be identified as the cause for any particular event.

Prior to this hypothesis, Ferguson et al. (2014) evaluated the feasibility of detecting spacecraft charging and arcing by remote sensing. This was a broad study mostly directed at Geosynchronous Earth Orbit (GEO) satellites in the general context of spacecraft charging (not specifically arc-induced contamination), but the authors estimated that the optical emission from an electrostatic discharge (ESD) on a GPS solar panel would be detectable at the $\sim 10\sigma$ level with a 1m telescope. Other methods of detection were addressed, such as radio emission of ESD, optical glow and Bremsstrahlung X-rays from electron impact, and optical afterglow of ESD. Ultimately, only the microsecond optical and radio bursts from ESD hold any promise of being detected from the ground.

Ferguson et al. (2017) reported initial results of their ground based observing campaign to detect the optical and radio signals of arcing of GPS satellites. Radio data obtained with the 305m Arecibo telescope showed differences between on- and off-source signals, consistent with pulsed emission from the GPS of $\sim 140\mu\text{s}$ duration. With no optical detections with their 3.5m telescope, the radio events could not be attributed to arcs. However, they also provided details on the maximum arc energy possible for each generation of GPS as well as a quantitative estimate of the efficiency loss per arc, which would be useful in determining if an observed arcing rate is consistent with the enhanced panel degradation rate. They estimate that an arc rate of 1-2 arcs per hour would account for the observed degradation rate.

1.5 Expected Signal

The maximum arc energy can be calculated from $E = 1/2CV^2$, where C is the panel capacitance and V is the arc voltage. With values of $C = 2.33\mu\text{F}$ and $V = 300\text{V}$ for Block II-R satellites (Table 3, Ferguson et al. 2016), the maximum arc energy is 0.10J. Assuming 7% of the arc energy is emitted as photons (typical of arc lamp efficiency) and a mean wavelength of 500 nm (4×10^{-19} J per photon), there should be $\sim 1.75 \times 10^{16}$ photons generated per event. If these photons are emitted over 4π steradians, the flux on the ground would be 10.7 photons/m². The 6.5m MMT would therefore collect ~ 356 photons per event, less transmission losses through the atmosphere and telescope.

A calorimetric study of the optical emission of ESD by Kucerovsky et al. (2002) observed a 2.9mJ emission for a 46.9mJ arc, an efficiency of $\sim 6\%$. While the assumption of 7% efficiency is reasonable based on available information, it is the largest source of uncertainty in expected arc signal.

An arc emission has a duration on the order of microseconds, so the best observing strategy would call for the fastest possible frame rate to keep sky background to a minimum while maintaining a duty cycle as close as possible to 100%. Ferguson et al. (2016) state arc rates of 1.65 and 1.32 arcs per hour for Block II-R and II-F satellites respectively, which bodes well for an arc occurring during the $\sim 40 - 50$ minute eclipse duration. However, this assumes the best case scenario that each arc fully discharges. Many GPS satellites carry sensors as part of the United States Nuclear Detonation Detection System (USNDS) to detect the radio emissions of nuclear explosions. Ferguson et al. (2017) studied whether the event rate of anomalous, undispersed radio signals not attributable to distant sources was consistent with expected arc rates. They found that this could be true if arcs only partially discharge, meaning arcs are optically fainter, but more frequent.

Chapter 2

Observing Strategy

*If we can hit that bull's-eye, the rest of
the dominoes will fall like a house of
cards. Checkmate.*

–Zapp Brannigan

This project aimed to detect the optical emission of arcing events on GPS solar panels. To do this, the satellite must be observed when it passes through Earth's shadow. During eclipse, the satellite will not be visible; only arcing events should allow the satellite to be detectable. An arc would be seen as a statistically significant increase in flux in a single exposure. It is highly unlikely that any astronomical transient would produce the same effect at the exact time and position of the satellite, and cosmic rays are easily identified by saturated count levels and pixel structure inconsistent with the PSF.

To maximize the probability of detecting an event with significant SNR, a large photon collector and a sensitive, high speed detector with negligible dead time between exposures are required. These requirements are met by the combination of the 6.5m MMT Telescope and a Princeton Instruments Electron Multiplying Charged-Coupled Device (EMCCD) camera.

2.1 The MMT and Red Channel Spectrograph

The MMT (Figure 2.1, formerly Multiple Mirror Telescope, now simply MMT following replacement of the six 1.8m primaries with a single 6.5m primary), operated by the University of Arizona and the Smithsonian Institution, is located at the Fred Lawrence Whipple Observatory on Mt Hopkins, Arizona, USA. It can operate with three secondary mirror configurations: f/9, f/5, and an adaptive f/15 secondary. This project made use of the Red Channel Spectrograph (Schmidt et al., 1989) utilizing the f/9

secondary. The Red Channel, and its counterpart Blue Channel, form a two-beam low-to-moderate resolution spectrograph. The Red Channel dewar was replaced with the EMCCD detector, and the spectrograph operated in direct imaging mode.

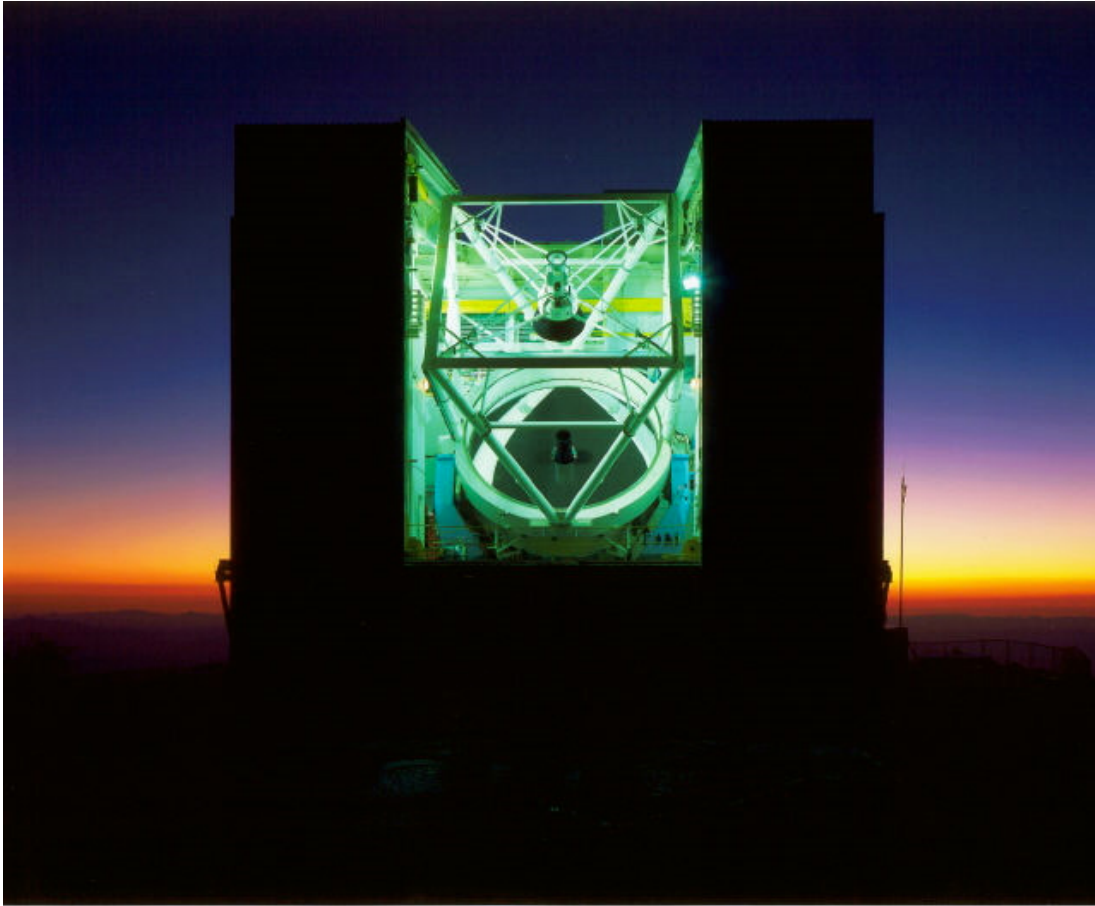


Fig. 2.1 — The MMT at Mt Hopkins, Arizona. Image courtesy of MMTO.

2.2 EMCCD Detector

With an arc duration much shorter than the minimum possible exposure time, it is impossible to time resolve the optical emission. However, the shortest possible exposure time is still required to keep the sky background to a minimum; the arc will contribute a given number of photons to any exposure longer than the event time, while sky background will continue to accumulate. This is balanced with the shortest possible readout time to minimize (or eliminate) dead time between frames. To this end, a Princeton Instruments ProEM-HS:512BX3 camera was employed. This camera contains a back-illuminated 512×512 Electron Multiplying e2v CCD97B with $16\mu\text{m} \times 16\mu\text{m}$ pixels. It offers a Frame Transfer mode, where a completed exposure is transferred from the active sensor area to a frame transfer area for readout, which frees the active area for the

next exposure to start immediately. This means that as long as the exposure time is longer than the readout time, there is zero dead time between exposures. The camera also offers on-chip electron multiplication (EM), which multiplies the pixel charge generated by the incoming photons. This allows detections at very low light levels, but more importantly effectively reduces the read noise by the EM gain:

$$SNR = (S * QE) / \sqrt{([S + B] * QE * F^2) + (D * F^2) + (\sigma_R / G)^2} \quad (2.1)$$

where S is the source photons, B is the background, QE is the detector quantum efficiency, G is the EM gain, D is dark current, σ_R is read noise, and F is the excess noise factor accounting for the probabilistic nature of electron multiplication.

2.3 The Optomechanics

Ideally, the EMCCD detector would be placed at the same position as the Red Channel detector, but the Red Channel’s design makes this impossible (Figure 2.2). The Red Channel detector is contained within the dewar’s “snout”, protruding into the folding flat mirror (Figure 2.3). The EMCCD housing is too large to be accommodated, so the focus was relayed to the EMCCD using a Thorlabs MAP103030-A 1:1 achromatic pair relay lens, also requiring a SM1A39 C-mount to SM1 adapter.

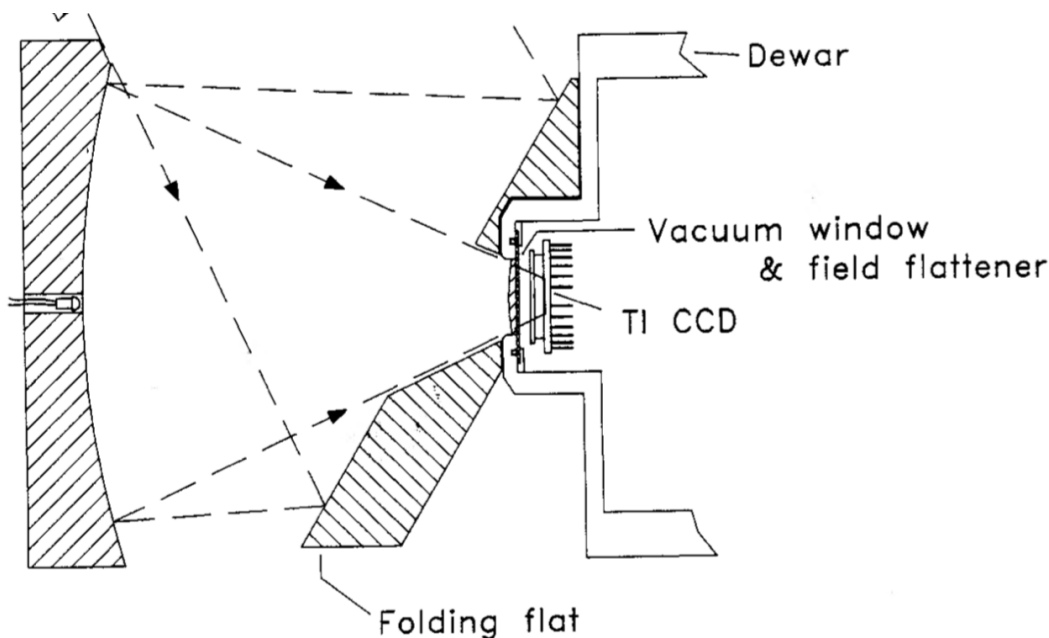


Fig. 2.2 — Schematic of the Red Channel camera. (Schmidt et al., 1989)

A custom mounting bracket was designed and fabricated to attach the EMCCD to the Red Channel dewar mount (Figures 2.4 and 2.4). The location of the Red Channel

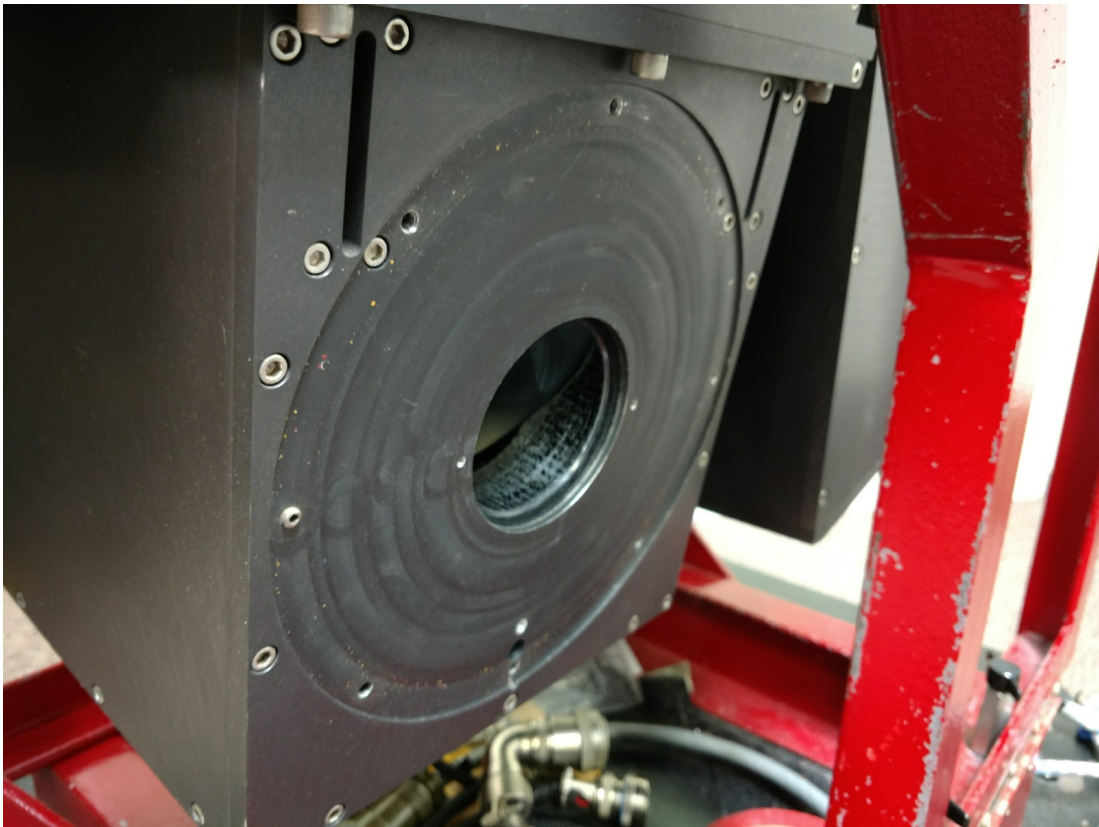


Fig. 2.3 — Mounting surface of the Red Channel dewar. Image courtesy of Will Goble, MMTO.

detector was not precisely measurable, so some z-axis range was incorporated into the bracket design for gross focus adjustments.

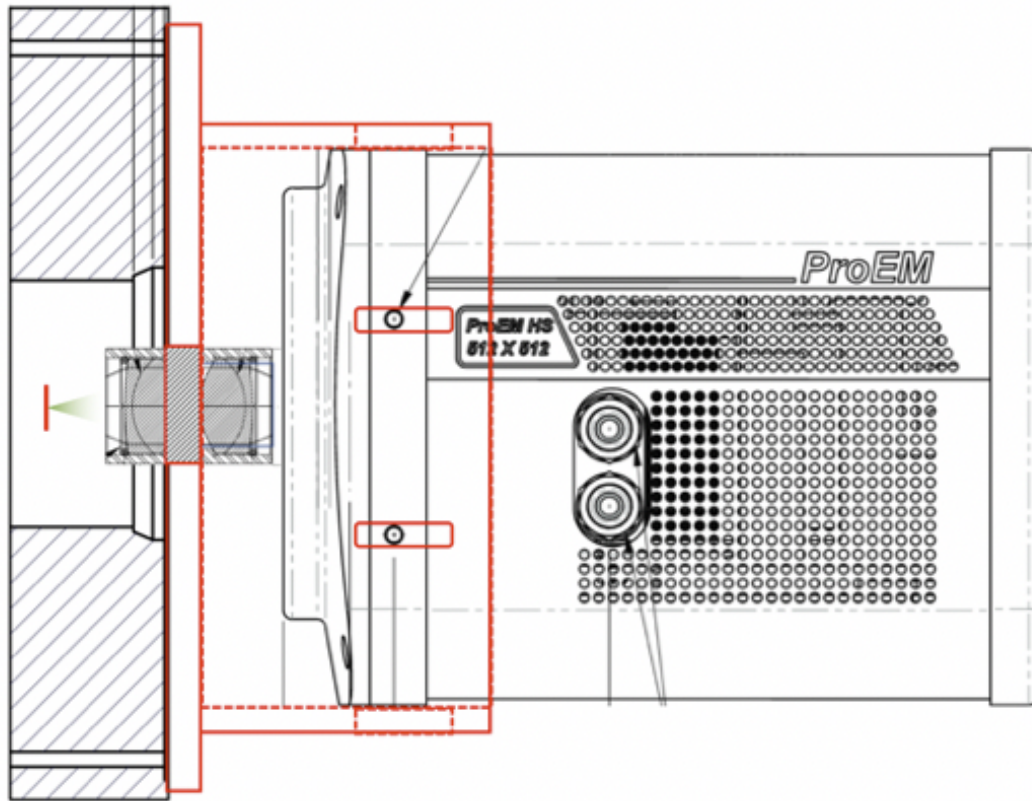


Fig. 2.4 — Mockup of EMCCD interfaced with Red Channel.

At the Red Channel focus, the image scale is $50\mu\text{m}/''$ (Schmidt et al., 1989), which with $16\mu\text{m}$ pixels gives a pixel scale of $0.32''/\text{pixel}$ and a field of view $2.7' \times 2.7'$. This would provide for a well-sampled PSF, however as will be shown in Section ??, the final image quality does not warrant such a fine pixel scale. This allowed binning the detector array for faster readout without undersampling the PSF.

2.4 Benchtest

2.4.1 Relay Lens Quality

In order to avoid any surprises at the telescope, the lens and camera were tested in the lab. First, an on-axis point source was simulated using a white light beam collimated from a $10\mu\text{m}$ pinhole, and focused through a microscope. The image was moved through focus until the sharpest image was obtained. The measured full width at half maximum (FWHM) is ~ 2 pixels, or $32\mu\text{m}$ (Figure 2.6). The diffraction limit at the d wavelength (587.56nm) for a 22.9mm entrance pupil is $25\mu\text{m}$.

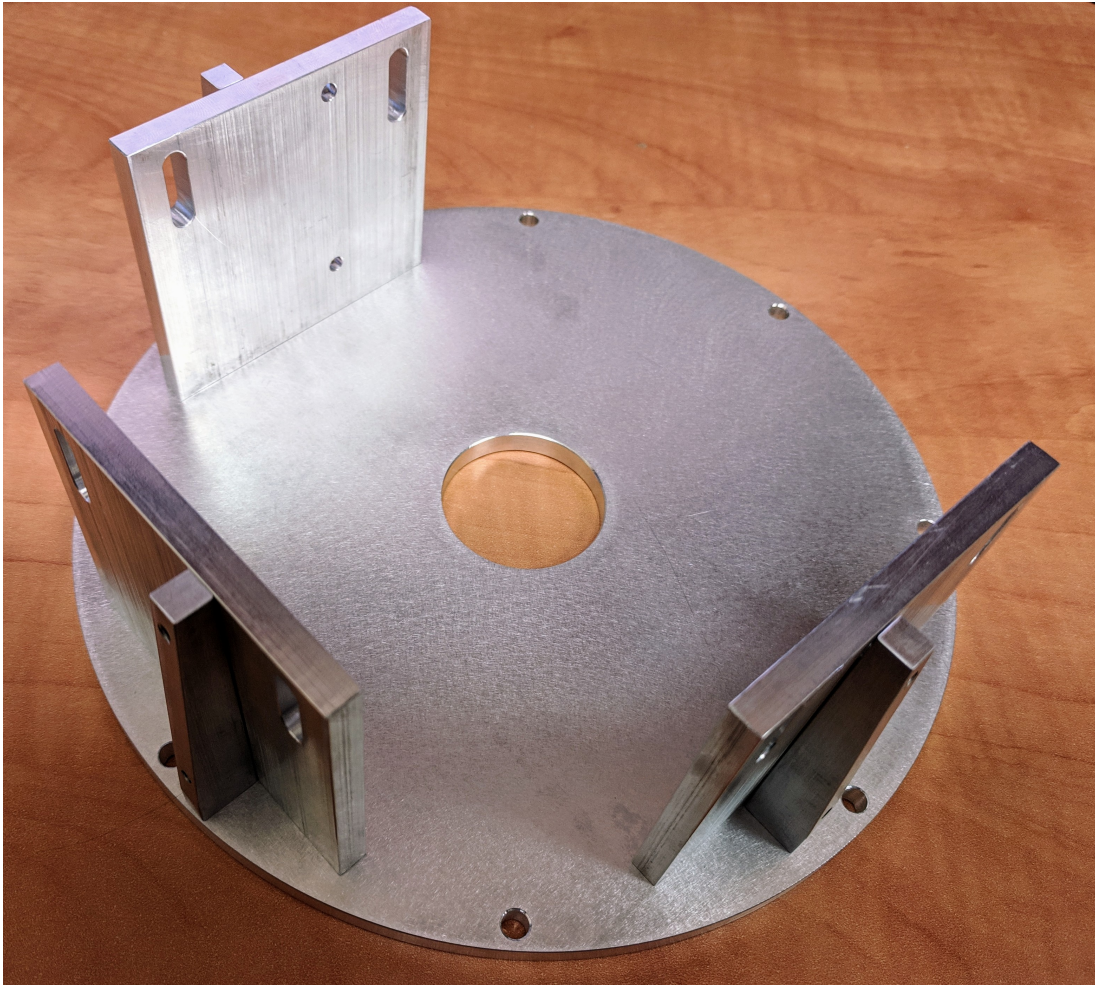


Fig. 2.5 — The completed bracket, fabricated in the Steward Observatory machine shop.

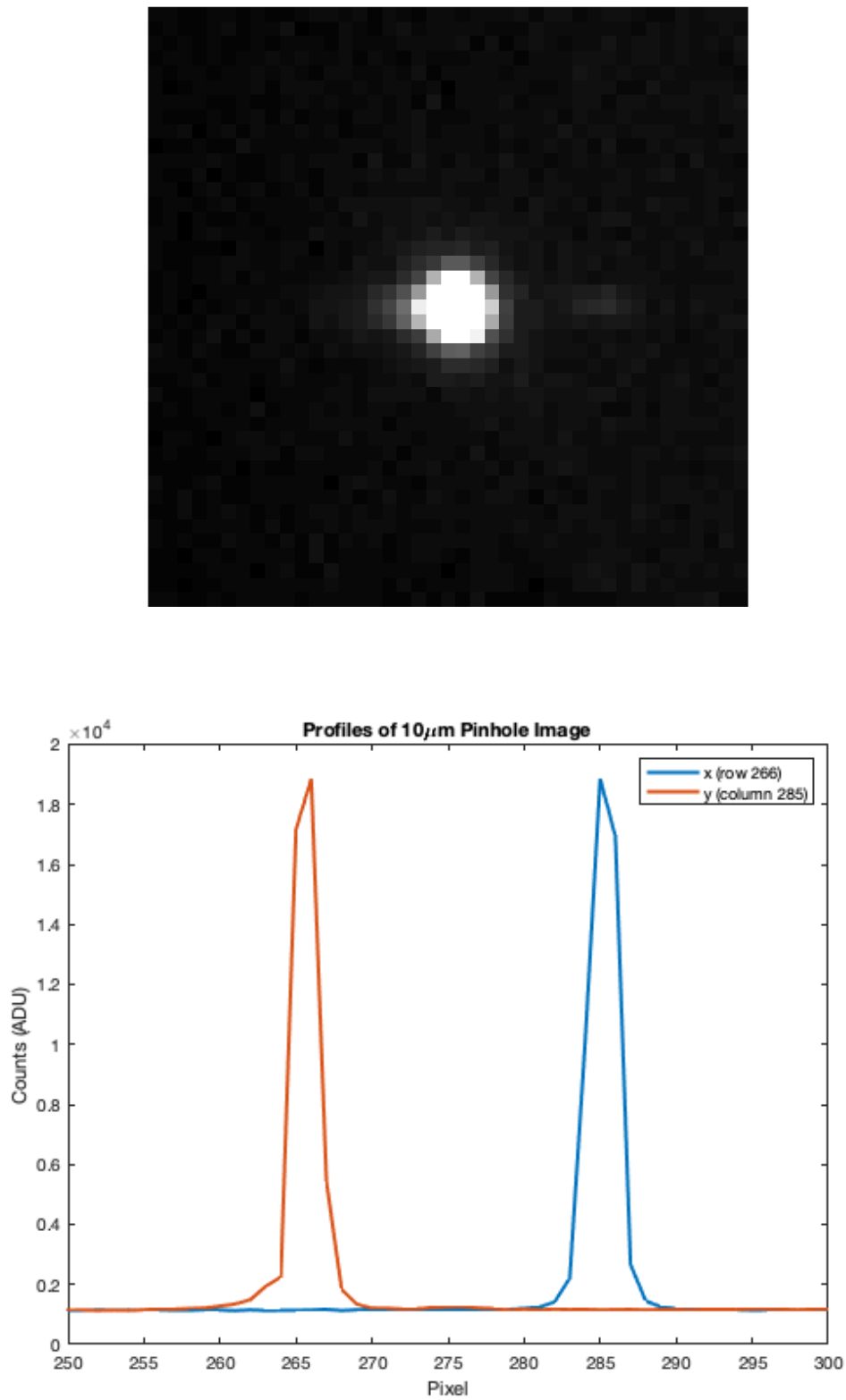


Fig. 2.6 — *Top*: Focused image of 10μm pinhole. *Bottom*: PSF profiles in x and y direction. The FWHM is ~ 2 pixels, or 32μm.

Using a scale model of the Red Channel focal plane (Figure 2.7), the field of view and image quality were assessed. Figure 2.8 shows the images of the model through the lens with 1×1 and 2×2 binning. The oscillations that appear on the edges of the black regions are printer artifacts. Note the printer was also unable to reproduce the numbers present in the original image. The 2×2 binned image is not discernably degraded from the full frame 1×1 binned image, but operating in this mode will reduce readout time and readout noise.

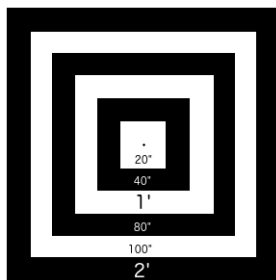


Fig. 2.7 — Imaging target simulating plate scale of MMT Red Channel detector. The 2 arcminute box is $8 \text{ mm} \times 8 \text{ mm}$.

2.4.2 Detector Quality

The ProEMCCD offers a traditional CCD mode (Low Noise) and the Electron Multiplied (EM) mode. The Low Noise mode is unsuitable for this experiment as the minimum readout time for a full frame is $\sim 300\text{ms}$ and the expected arc signal would be swamped by sky background. With the EM mode, the readout time is reduced to $\sim 30\text{ms}$ (even less with binning), as well as effectively reducing the readout noise through the EM gain, increasing SNR.

With the EM mode, the camera offers 5MHz, 10MHz, and 20MHz readout rates. The 20MHz setting appeared unstable and introduced random artifacts to the images: alternating bright and dark pixels sprinkled across the array. Therefore, only the 5MHz and 10MHz rates were considered. The camera also offers three analog gain settings: Low, Medium, and High, with nominal gains of 12, 6, and $3 \text{ e}^-/\text{ADU}$ respectively for the EM mode. The readout noise for each of these modes was measured by taking the averages of nine bias exposures and subtracting this from a tenth exposure. The results are presented in Table 2.1.

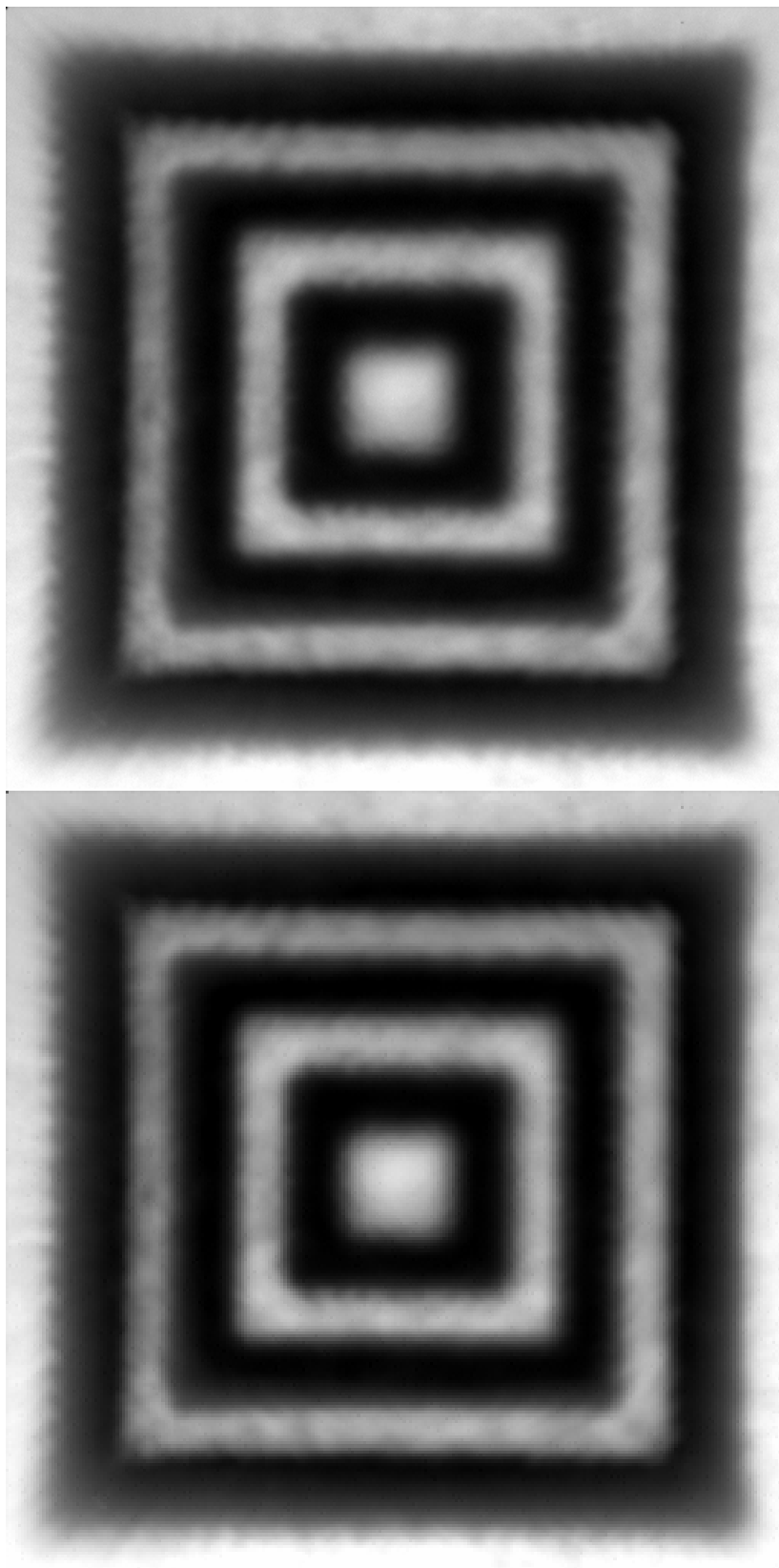


Fig. 2.8 — Imaging target imaged through relay lens with 1×1 binning (top) and 2×2 binning (bottom). The outer edge of the outermost square is 2 arcminutes.

| RON (e ⁻) | Low | Medium | High |
|-----------------------|-----|--------|------|
| 5 MHz | 55 | 44 | 45 |
| 10 MHz | 78 | 67 | 67 |

Table 2.1 — Measured readout noise for various modes.

In order to set expectations, the SNR of arcs of varying intensities with an estimated sky background was calculated. The combination of the relay lens and camera operate from $\sim 400-900\text{nm}$, spanning the *BVRI* filter system. There is overlap between filters and non-unity transmission across this wavelength range, but a first order estimate of the sky background can be made by summing the sky fluxes in each band. A literature search revealed only *V* and *R* measurements of Mt Hopkins (Massey & Foltz, 2000), but Pedani (2009) measured the sky brightness of Mt Graham (a site also in southern Arizona) in *UBVRI*. These measurements were taken in new moon conditions and at solar minimum, so represent the darkest possible sky. Mt Hopkins is also closer to population centers and will have brighter skies (this is reflected in comparing the *V* and *R* measurements between sites), so 1 mag/sq'' is added to the published values to allow for this.

The values for sky brightness for each band, in magnitudes per square arcsecond, were converted to fluxes in $\text{W/m}^2/\mu\text{m}$. Each flux value was converted to a number of photons/s/m² using the photon energy at each band’s effective wavelength. This was then scaled by the MMT’s collecting area, a rough bandwidth of each band, and finally by the pixel size (0.64×0.64 arcsec for 2×2 binning) to get the number of photons/s/pixel. The total estimate is ~ 6700 counts/s/pixel. See Table 2.2 for a summary.

| Band | Sky Brightness (mag/sq'') | Flux ($\text{W/m}^2/\mu\text{m}$) | Effective Wavelength (nm) | Bandwidth (μm) | Counts (ph/s/MMT/pix) |
|--------------|---------------------------|-------------------------------------|---------------------------|-----------------------------|-----------------------|
| B | 21.8 | 1.3×10^{-16} | 433 | 0.1 | 376 |
| V | 20.8 | 1.8×10^{-16} | 550 | 0.1 | 661 |
| R | 19.8 | 2.2×10^{-16} | 700 | 0.2 | 2055 |
| I | 18.8 | 3.0×10^{-16} | 900 | 0.2 | 3604 |
| Total | | | | | 6695 |

Table 2.2 — Values used to estimate sky background.

The Electron Multiplication of the EMCCD allows detection at very low light levels, but it will also multiply the sky background. To explore the effect of EM Gain, the SNR as a function of EM gain and arc brightness was calculated and is shown in Figure 2.9. To calculate the SNR, the sky count rate was assumed to be 6695 ph/s/pixel, readout noise $67e^-$, exposure time 8ms, 25 pixel measurement area, and excess noise factor

1.4. This excess noise factor is to account for the increase in noise when using EM as the process of electron multiplication is probabilistic. A Princeton Instruments Tech Report (2016) states that this value ranges from 1 – 1.4 for EM gain values as high as $1000\times$, so the worst case value of 1.4 was used. This increase in noise is more than made up for with the effective reduction in readout noise. From Figure 2.9 it can be seen how valuable the boost in SNR is: an arc event of 150 photons would be a non-detection without EM gain, or a detection of over 5.5σ with an EM gain of $100\times$.

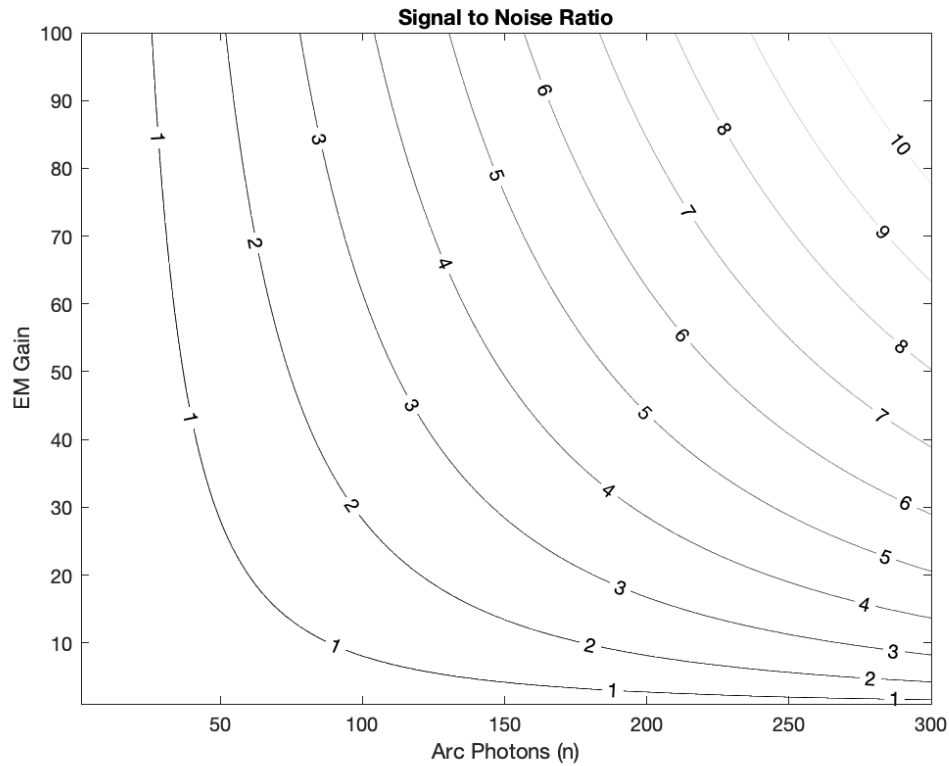


Fig. 2.9 — Signal to Noise Ratio as a function of arc counts and EM gain, assuming sky count rate of 6695 ph/s/pixel , readout of noise of $67e^-$, 8 ms exposure, excess noise factor $F=1.4$, and signal measurement over 5×5 pixel area.

Chapter 3

Results

*I've worked in the private sector,
they expect results.*

–Ray Stantz, PhD

This project was allocated a total of four nights at the MMT: 20190102 and 20190111 for engineering and testing, and 20190112-13 for science. Unfortunately, for all nights but 20180111, the MMT remained closed due to weather. Three eclipsing satellites were visible to the MMT during this night: NAVSTARs 48, 59, and 65 (Table 3.1). NAVSTAR 48 was concurrently observed by the Arecibo radio telescope; coincident optical and radio detections would constitute a slam-dunk arc detection.

3.1 Data Acquisition

On the night of 20190102, the EMCCD was successfully mounted to the Red Channel Spectrograph (Figure 3.1), the power supply and pass through network cable connected, and the camera operated from the control room. The initial gross focus was found by moving the detector in and out along the optical axis using the slotted mounting holes. Fine focus was then achieved through the Red Channel collimator. Best focus was found at the limit of the mounting holes, so in the intervening nights, these were extended for increased range in the event thermal conditions changed sufficiently to push focus beyond the initial reach.

| Name | NORAD ID | Block | Panel Size (m ²) | Maximum Arc E (J) | Umbra (UTC) |
|------------|----------|-------|------------------------------|-------------------|---------------------|
| NAVSTAR 48 | 26407 | IIR | 13.8 | 0.10 | 04:36:16 - 05:13:13 |
| NAVSTAR 59 | 29601 | IIR-M | 13.8 | 0.10 | 08:00:35 - 08:41:28 |
| NAVSTAR 65 | 36585 | IIF | 6.0 | 0.034 | 08:55:10 - 09:43:52 |

Table 3.1 — Target information and eclipse times.



Fig. 3.1 — The EMCCD mounted to the Red Channel.

The first night of the three night run from 20190111-13 was the only chance for the telescope to open. Conditions were clear and sky flats were obtained during twilight, as much to test the camera operation as for calibration purposes. These were taken in “Low Noise” mode (no EM gain) and 1×1 binning. Ultimately these flats were taken in a different configuration than the GPS observations, so they were only used for correcting the standard star observations taken with the same configuration.

Once the sky was dark enough, the telescope was slewed to the first target, NAVSTAR 48. The MMT can track non-sidereal targets using Two-Line Element sets (TLE) and does so routinely, so this required no special preparation. The target was confirmed visible and showed acceptable drift within the field of view. While observing the satellite, the detector parameters were tweaked, settling upon 4×4 binning with an EM gain of $100\times$, as well as a sub array readout to discard non-illuminated pixels. This allowed for a readout time of 7.986 ms with a pixel scale that somewhat undersampled the PSF but not sufficiently so that a cosmic ray could mimic an arc.

With ample time before the satellite would enter eclipse, a spectrophotometric standard star (Hz 14, Massey et al. 1988) was observed to relate the observed flux to absolute flux. Five exposures in Low Noise mode with a 3 second exposure time were obtained.

Observation of NAVSTAR 48 began at 04:33:33 UTC on January 12, 2019 and concluded at 05:17:01. The satellite entered umbra from 04:36:16 and exited at 05:13:13. At a sampling rate of 122 Hz, a total of 318,484 images were acquired, with the satellite successfully recovered within the field of view upon egress from umbra.

The second target was NAVSTAR 59, with data acquisition beginning at 07:49:05 and concluding at 08:44:13. Umbra began at 08:00:35 and concluded at 08:41:28. This observation was complicated by the telescope rotator approaching its limit, requiring unwrap during the sequence at 08:24. Unfortunately this put the satellite outside the field of view at the end of eclipse, meaning its position during eclipse could not be interpolated.

Observation of the final target, NAVSTAR 65, began at 08:51:14 and concluded at 09:44:15. Umbra began at 08:55:10 and ended at 09:43:52. This acquisition sequence was interrupted by a shutter closure of the Blue Channel spectrograph, which had to be operated manually in order to keep light passing through the system. Aside from a loss of ~ 30 s of eclipse coverage, this did not complicate analysis of the images.

An unfortunate oversight of data acquisition was that as the camera control computer was not internet-connected, its time was not synced. It ran 6s faster than the time displayed by the United States Naval Observatory (USNO). This was a visual comparison, so any times presented are accompanied with an uncertainty of ± 1 s.

3.2 Data Processing

The Red Channel produced uneven illumination across the detector, with a $\sim 5\%$ off-center radial gradient. The twilight flats obtained were using a different detector configuration than the GPS observations, but were used to flatfield the standard star observation. These flats were combined in the conventional manner: each was normalized by its median, then these were all median combined and normalized again by the maximum value.

To flat-field the satellite images, a super-flat was constructed from the data. Using 10,000 images evenly spaced through time, each image was normalized by its median, and then all 10,000 images median combined. For good measure, this was repeated a further four times with different sets of images, and then these five flats were medianed into a super flat. During the analysis detailed in section 3.4, each satellite image is bias subtracted and divided by the superflat. The detector was cooled to -70°C so dark current was negligible at $0.01\text{e}^-/\text{s}/\text{pixel}$.

3.3 Sensitivity

The spectrophotometric standard star Hz 14 was observed in order to estimate absolute sensitivity. This result is presented first as it has profound implications on all following results. Massey et al. (1988) contains the tabulated magnitude m versus wavelength λ , as well as an equation to convert this to number N_λ of photons/s/Å arriving at a 1 m telescope:

$$N_\lambda = \frac{4.5 \times 10^{10}}{\lambda} 10^{-[m+A_\lambda X/2.5]} \quad (3.1)$$

where A_λ is magnitudes of extinction per airmass and X is the airmass.

Figure 3.2 shows the published Hz 14 spectrum, the spectrum after atmospheric extinction at the observation airmass of 1.08, as well as the spectrum multiplied by the relay lens transmission specified by Thorlabs, and the EMCCD quantum efficiency (QE) from Princeton Instruments. The extinction coefficients of Mauna Kea were used, which showed agreement with modelled transmission from MODTRAN. The EMCCD QE was visually extracted from graphical data as tabulated data were not available. The three functions were resampled to a commonly spaced wavelength scale. Most transmission loss is blueward of 4000\AA where both the lens transmission and EMCCD QE drop off rapidly (Fig 3.3).

The overall transmission loss was calculated by integrating the post-extinction Hz 14 flux spectrum to determine the number of counts per second per 1m telescope. This was then scaled to the MMT collecting area: the area of the 6.5m primary minus the 0.9m central obscuration. The total flux expected to cross the MMT aperture from 400nm–800nm was 2.59×10^6 photons/s.

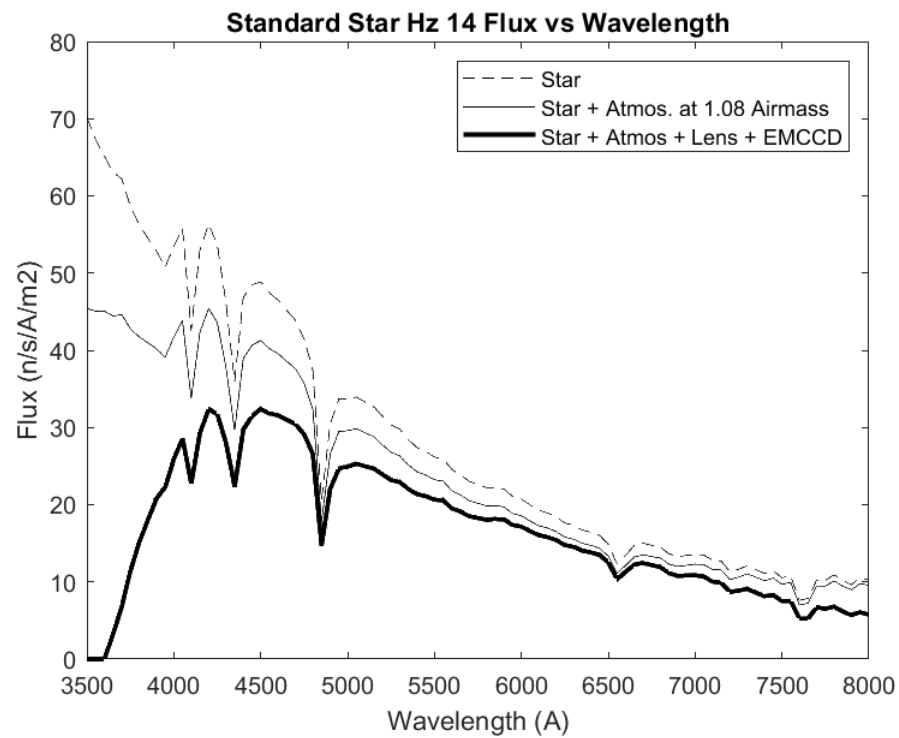


Fig. 3.2 — Number of photons/s/Åmm² vs wavelength for Hz 14 spectrum. Dashed line is from Massey et al. (1988), solid line includes relay lens transmission and EMCCD quantum efficiency losses.

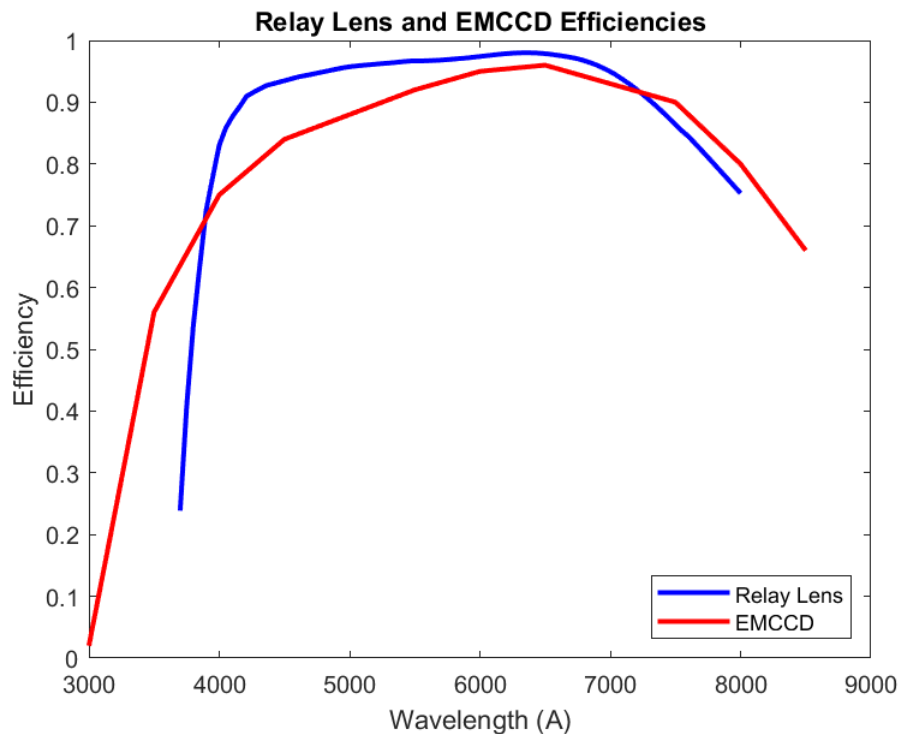


Fig. 3.3 — Relay lens transmission and EMCCD quantum efficiency versus wavelength.

The total detected stellar counts for each of the five flat-fielded images were calculated by summing the counts in a 70×70 pixel box centered on the star, and subtracting the total counts from a 70×70 box away from the star (Figure 3.4). The mean background-subtracted stellar counts was 2.45×10^6 ADU, which multiplied by the Low Noise mode high gain of $0.8e^-/\text{ADU}$ and divided by the exposure time of 3s, gives 6.53×10^5 photons/s, or a transmission loss of 74.8%.

The contribution from the relay lens and detector QE can be factored out by repeating the calculation using the spectrum after multiplication by the lens transmission and detector QE. This yields a transmission loss of 69.4% from the telescope and Red Channel optics in the 400nm–800nm range of interest. With a total of six reflective surfaces (including the MMT primary and secondary) and three refractive elements between the sky and the relay lens, an average efficiency of 89% per surface would account for such losses. Schmidt et al. (1989) provides transmission measurements of the Red Channel, with a peak of $\sim 25\%$, however these measurements include the grating and old Red Channel CCD QE, which were not used for this experiment, and were taken before the MMT’s upgrade to a single primary mirror. Nonetheless, it illustrates that while disappointing, the low measured transmission is not unprecedented.

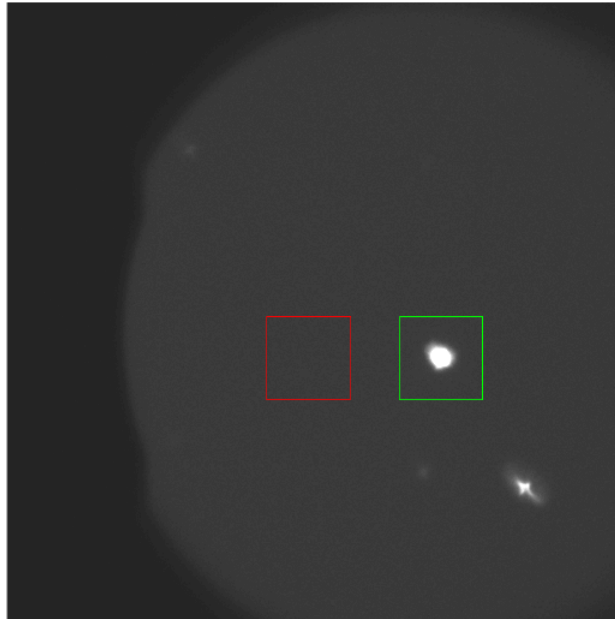


Fig. 3.4 — Raw image of Hz 14. Green box shows pixels used to calculate total star counts, red box shows pixels used to calculate sky counts. These calculations were done on the flat-fielded images.

3.4 Detection Algorithm

The expected signal from an arc is a single-frame jump in flux at the position of the satellite. From the pre- and post-eclipse pixel position of the satellite, the position as a function of time was linearly interpolated. There was some drift on the order of $40''/\text{hr}$, due to telescope tracking errors, TLE uncertainty, or both. Stars or other objects will remain relatively stationary between sequential frames, so this can be used to mask them out. Five sequential images are flat-fielded and smoothed with a 1.5 pixel width Gaussian (roughly the PSF). These five images are then median combined into a single image, where stars or objects present in all 5 images will remain, while arcs (or cosmic rays, etc.) will be medianed out. The median and standard deviation of this new image are calculated after clipping the brightest 10% of pixels to avoid influence of bright stars. A binary mask is generated where any pixel 5σ above this median is set to zero, and all other pixels set to 1. This mask is then run through a 5×5 moving-minimum to expand the masked regions outwards by 2 pixels, ameliorating the edge effects of bright objects and the slight motion of stars between frames.

Cycling through each of the five images, the median and standard deviation were found for all pixels not masked. An edge mask was then applied to discard a 5 pixel border around the image where image quality and stars at the edge can generate false positives. With this final masked image, any statistically significant signals detected are from fluctuations present in no more than two of the five images. The next five images

were analyzed until the sequence is complete. Figure 3.5 shows a visual flow of the algorithm, with a simulated arc (see Section 3.5) inserted into real data. Determination of a robust detection limit is discussed in Section 3.5.

3.5 Monte Carlo Simulation

To determine the optimum detection limit and efficiency of the algorithm, artificially generated arcs and backgrounds were analyzed with the same method. The PSF of the system was approximated by fitting a 2D Gaussian distribution to a centrally located, sufficiently bright star from the observations. Then using this distribution, N arc photons were distributed on this image. A small random jitter was added to the central location of each iteration to avoid the arc center always occurring at the same intrapixel position. These photons were then converted to counts using EM gain = $100\times$ and analog gain = $3e^-/\text{ADU}$ and were then “imaged” into a 2D array.

The background was generated using a Gaussian distribution of counts, where the mean and standard deviation were calculated from 10,000 frames of the actual data: $\mu = 303$ ADU and $\sigma = 96$ ADU. This corresponds to a sky count rate of ~ 1136 ph/s/pixel, which after accounting for $\sim 75\%$ transmission losses is about $\sim 20\%$ of the sky background estimate in Section 2.4.2. Artificial arcs with photon levels from 0 to 120 in increments of 6 were run through the algorithm, with 10,000 iterations per level. Examples of these simulated images are shown in Figure 3.6.

For each image, the maximum significance above the image median was calculated for a 9×9 pixel box centered on the arc, as well as another 9×9 box of empty background. Figure 3.7 shows the distribution of these maximums versus number of detected arc photons, as well as the significance of “detections” in the blank background region. The solid lines are the means of these maximums (with $\pm 1\sigma$ for the arc detections), and the dashed lines indicate the spread: The dashed red lines are the mean ± 3 standard deviations of these maximums, and the dashed blue line is the background mean maximum $+4.5$ standard deviations. This value was chosen so that assuming Gaussian statistics, ~ 3 false detections would be expected per million images, or one per satellite observation sequence. It corresponds to a detection threshold of 4.7σ above the median within each individual smoothed image.

The fraction of arcs for each count level detected above 4.7σ is shown in Figure 3.8: 10% efficiency occurs at 38 arc photons, 50% at 50 arc photons, and 90% at 62 arc photons. It should be stressed that these are photons *detected*, not photons collected by the telescope. As was seen in section 3.3, transmission losses are as high as $\sim 75\%$, which would put the 10, 50 and 90% efficiencies at $\sim 152, 200$, and 248 photons respectively.

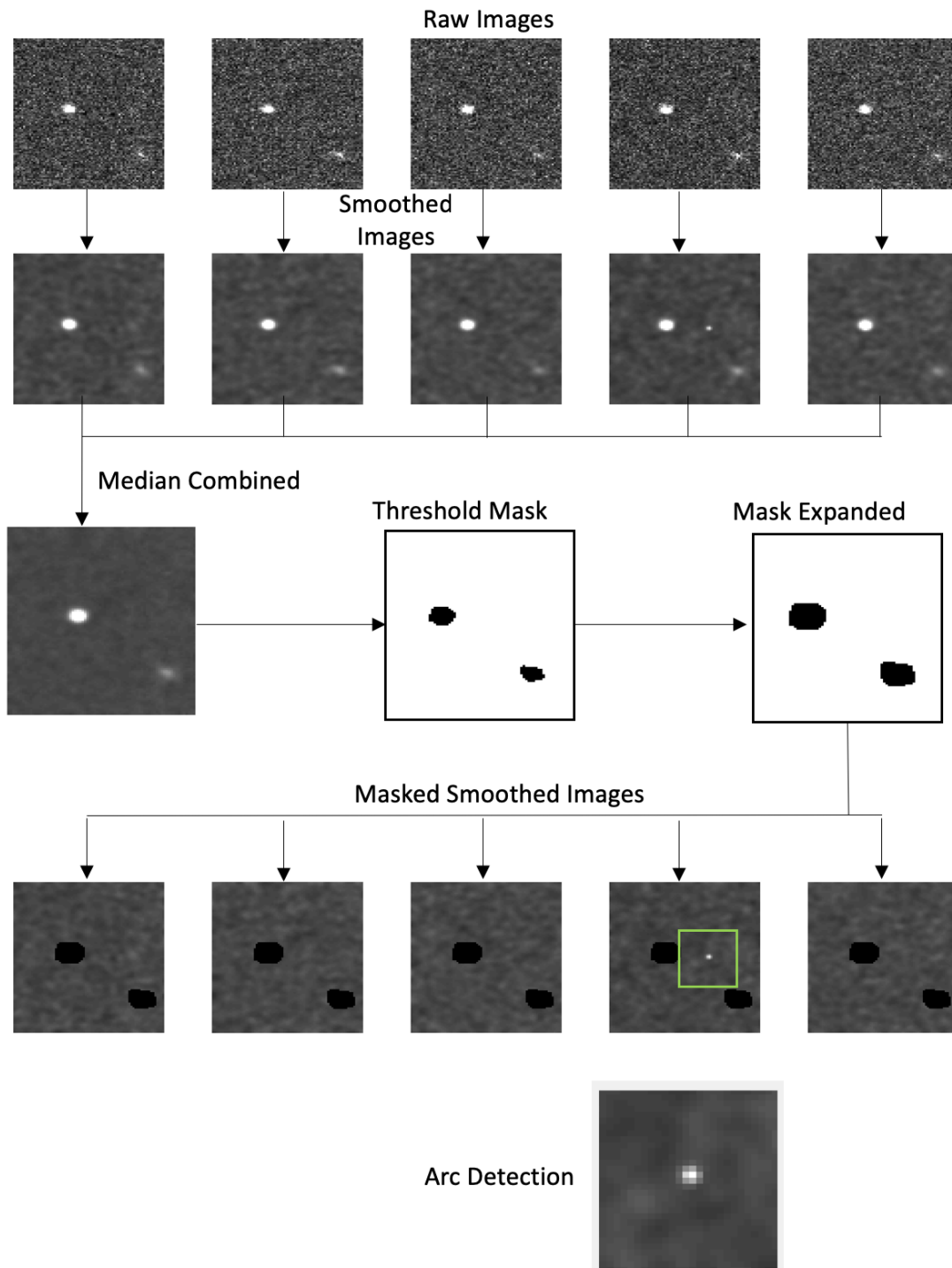


Fig. 3.5 — Detection algorithm flow. Five images are smoothed, median combined, and stars masked out. The mask is applied to the individual smoothed images, leaving only objects present in a single image to remain as a significant detection.

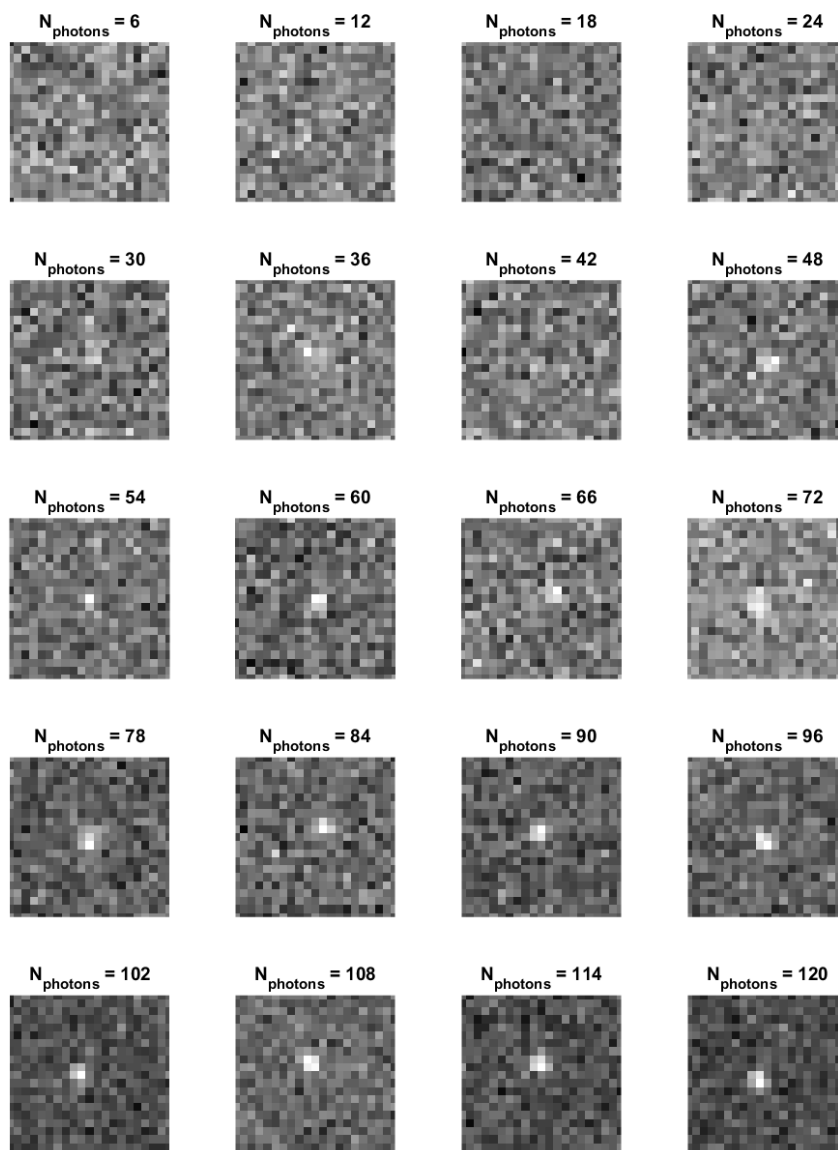


Fig. 3.6 — Simulated arcs for various numbers of photons.

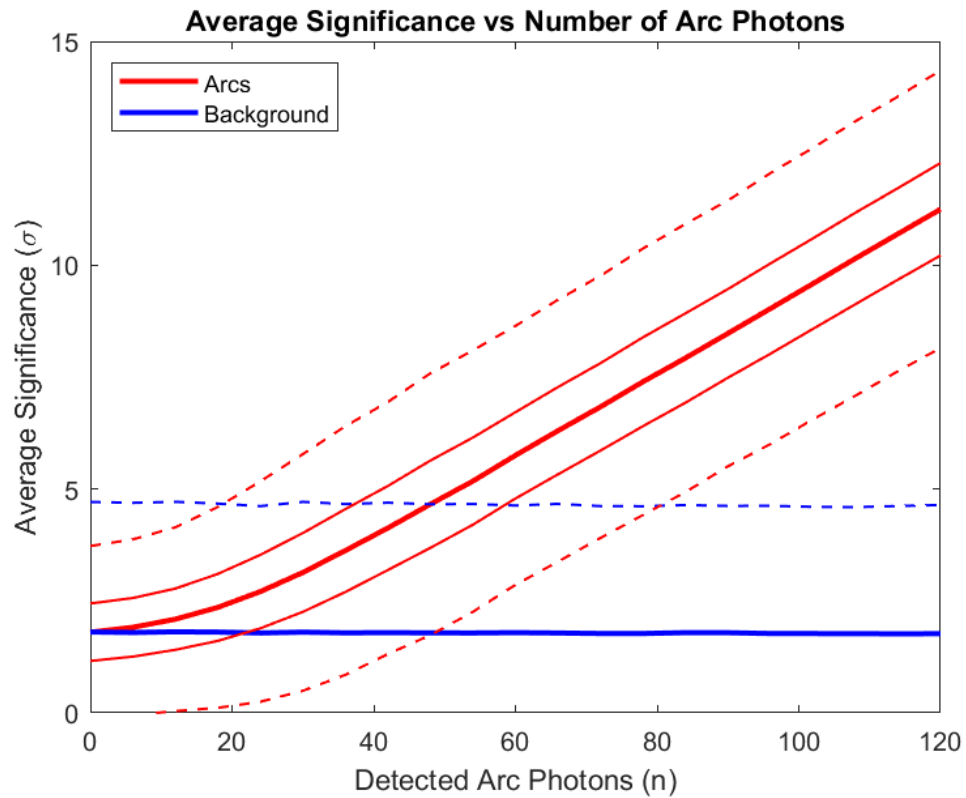


Fig. 3.7 — Detection significance versus arc photon count. The solid lines show the mean values for arcs (red) and background (blue). The dashed lines are ± 3 standard deviations for arc detections (not the same as σ on the y-scale) and $+4.5$ standard deviations for the background.

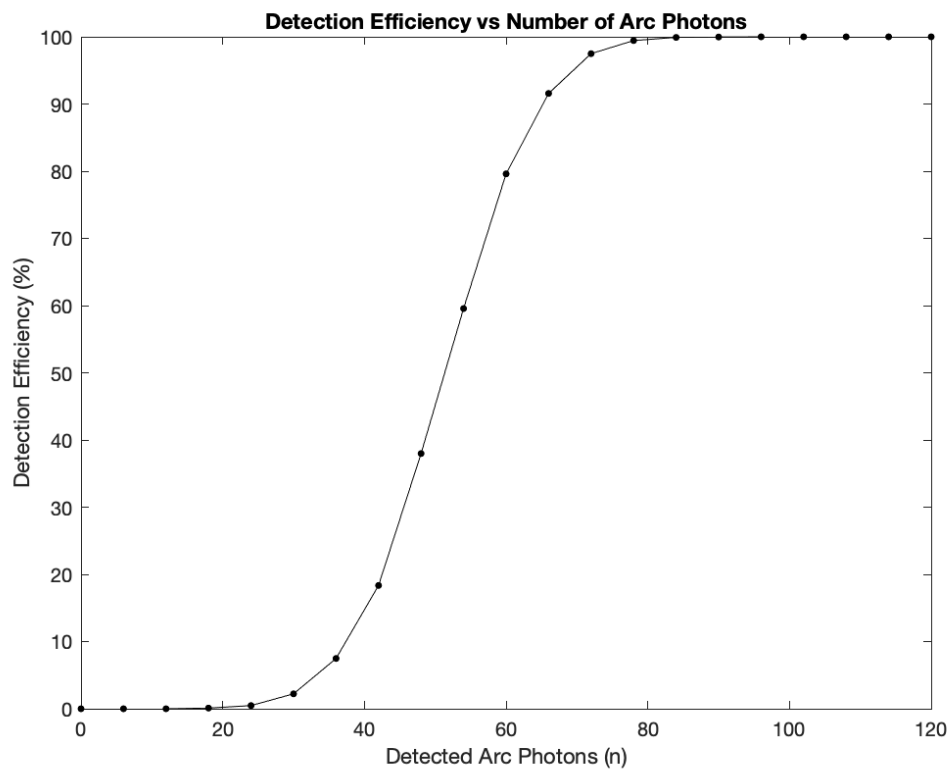


Fig. 3.8 — Fraction of simulated arcs detected versus arc photon count.

3.6 Results

3.6.1 NAVSTAR 48

Applying this method to NAVSTAR 48, 66 frames yield a brightness fluctuation above the 4.7σ threshold at the satellite position. One (image 241959) is very obviously a cosmic ray strike. Twenty-four are detections from the satellite pre- and post-eclipse, where the low illumination level places it at the limit of masking. Four are very bright star artifacts leaving 37 possible arc detections, many more than the ~ 1 false positive expected in Section 3.5.

To test the likelihood that these are arc detections, the analysis was rerun on a region of the images $\sim 50''$ away from the satellite’s interpolated path (Figure 3.9), yielding 86 total frames. After removing two cosmic rays and 35 bright star artefacts, 49 “arc” detections between 4.7σ to 5.92σ remain. Therefore, a significant fraction, if not all, of the candidate arcs are false positives. An example false positive is shown in Figure 3.10, detected at 5.7σ , greater than any detections at the satellite position. This negative result is further supported by the lack of time coincidence with Arecibo detections (Section 3.6.1).

A possible source of false positives above the threshold is that these frames were taken in instances of good seeing, pushing otherwise undetectable faint stars momentarily above the background, *a la* lucky imaging. The exposure time of 8ms is on the order of the atmospheric coherence time in the optical, so in the 318,484 frames taken it is feasible that occasionally a very faint star’s speckles align just so. With lucky imaging, frames are selected when chance dictates the speckles align. As the number of speckles is proportional to $(D/r_0)^2$, when the diameter D of the telescope increases, the chance of all speckles aligning decreases. To produce an “unlucky” image however, it is not required that all speckles align to produce good image quality, just that enough do to produce a momentarily detectable SNR. Therefore, the chance of this occurring would *increase* with the total number of speckles. A thorough statistical investigation would be needed to determine if this is a significant factor. The probability of an unlucky detection would be a function of the PSF, D/r_0 , the density of undetected stars just below the threshold, and the tracking rate.

This hypothesis can be tested, at least qualitatively, by stacking images to increase the SNR of stars. Using the cosmic ray detection in image #241959 as an example (a very strong signal with multiple faint stars), Figure 3.11 (top) shows the unsmoothed detection image, smoothed detection image, and a smoothed, stacked image constructed from 51 images (0.41s time span). Stars that are invisible in the individual images are clearly visible in the stacked image. This demonstrates that stars are lurking at the edge of detectability, and could be the cause of 7 of the 37 candidate detections as well as 6 of the 49 off-source false positives. Examining the stacked images also reveals



Fig. 3.9 — The interpolated path of NAVSTAR 48 during the observation period (green line) and the offset field searched for false positives (red box). The bright object at the start of the green line is NAVSTAR 49 before eclipse.

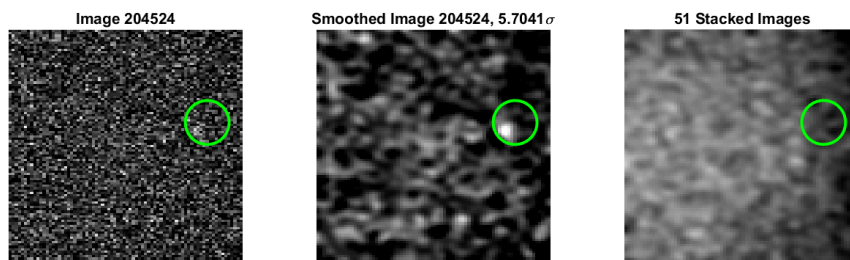


Fig. 3.10 — False positive detected away from satellite. Green circle is the blank area searched.

whether the satellite itself is producing the same effect as it enters and exits umbra (Figure 3.11, bottom).

Stacking the images also reveals another possible source of false positives: persistence. Figure 3.12 (top) clearly shows structure across the detector trailing the bright star as it exits the field of view. This may be the cause of the detection in image #171903 (Figure 3.12, bottom).

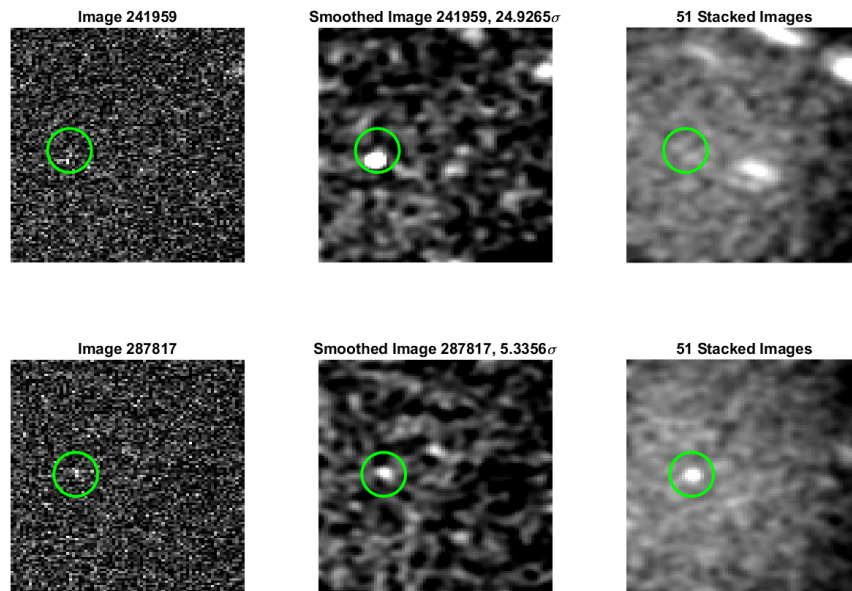


Fig. 3.11 — Image prior to detection, image of detection, image after detection, and stacked, smoothed image centered on detection. *Top*: In this case, the detection is a cosmic ray, but the background stars are clearly visible in the stacked image while invisible in the individual images. *Bottom*: Detection from image #287817 showing that the satellite is present in most or all 51 images, therefore is not an arc but rather the partially illuminated satellite exiting eclipse.

While faint stars and persistence may account for a few of the false positives, the mostly likely cause for the rest is simply that the assumption of Gaussian background noise is incorrect, therefore the threshold set too low. Despite the dubious nature of these arc candidates, they are of the expected significance so the details are presented in Table 3.2 and images in Appendix A. In short, no detections can be conclusively attributed to an arc without external confirmation, which may be possible from on-board telemetry. These detections range from 4.71σ to 5.57σ , corresponding to arcs of 20 to 90 detected photons, or 80 to 360 photons after transmission correction.

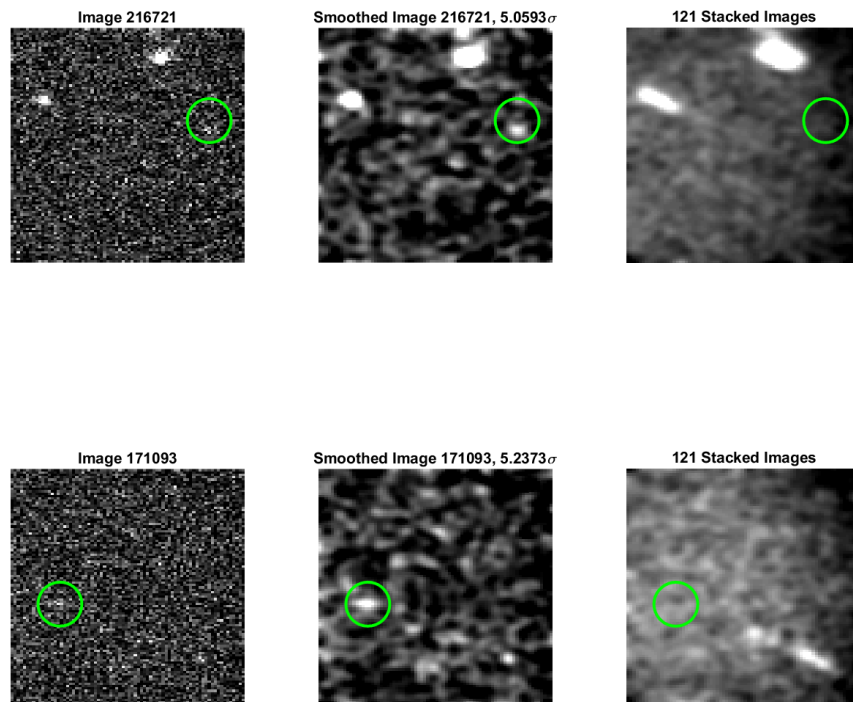


Fig. 3.12 — *Top*: Persistence caused by bright star (Taken from NAVSTAR 65 dataset).
Bottom: Possible NAVSTAR 48 false detection caused by persistence.

| Image # | Time (UTC \pm 1s) | Significance (σ) |
|---------|---------------------|---------------------------|
| 44580 | 04:39:37 | 4.93 |
| 57989 | 04:41:27 | 5.07 |
| 70143 | 04:43:06 | 5.08 |
| 82504 | 04:44:47 | 4.80 |
| 84908 | 04:45:07 | 5.57 |
| 93232 | 04:46:15 | 4.84 |
| 103634 | 04:47:40 | 4.79 |
| 112781 | 04:48:54 | 5.10 |
| 125487 | 04:50:38 | 4.72 |
| 129474 | 04:51:11 | 5.08 |
| 131175 | 04:51:25 | 4.83 |
| 140880 | 04:52:44 | 4.74 |
| 143282 | 04:53:09 | 4.73 |
| 147169 | 04:53:35 | 4.78 |
| 150458 | 04:54:02 | 5.15 |
| 171093 | 04:56:51 | 5.24 |
| 171355 | 04:56:51 | 4.73 |
| 173399 | 04:57:10 | 5.15 |
| 175336 | 04:57:26 | 4.84 |
| 196152 | 05:00:16 | 4.83 |
| 205732 | 05:01:34 | 4.97 |
| 208221 | 05:01:54 | 4.71 |
| 210015 | 05:02:09 | 5.08 |
| 211590 | 05:02:22 | 5.17 |
| 246346 | 05:07:06 | 4.75 |
| 254834 | 05:08:15 | 5.03 |
| 256342 | 05:08:28 | 5.06 |
| 256873 | 05:08:32 | 4.89 |
| 257058 | 05:08:33 | 4.90 |
| 263145 | 05:09:23 | 4.87 |

Table 3.2 — Candidate detections for NAVSTAR 48.

Comparison with Arecibo Results

NAVSTAR 48 was concurrently observed by the Arecibo radio telescope, providing a list of candidate arc event times (R. Rast, personal communication, April 4, 2019). The significance levels at the predicted satellite location versus image number (time) are shown for 2 second spans centered on these times in Figure 3.13.

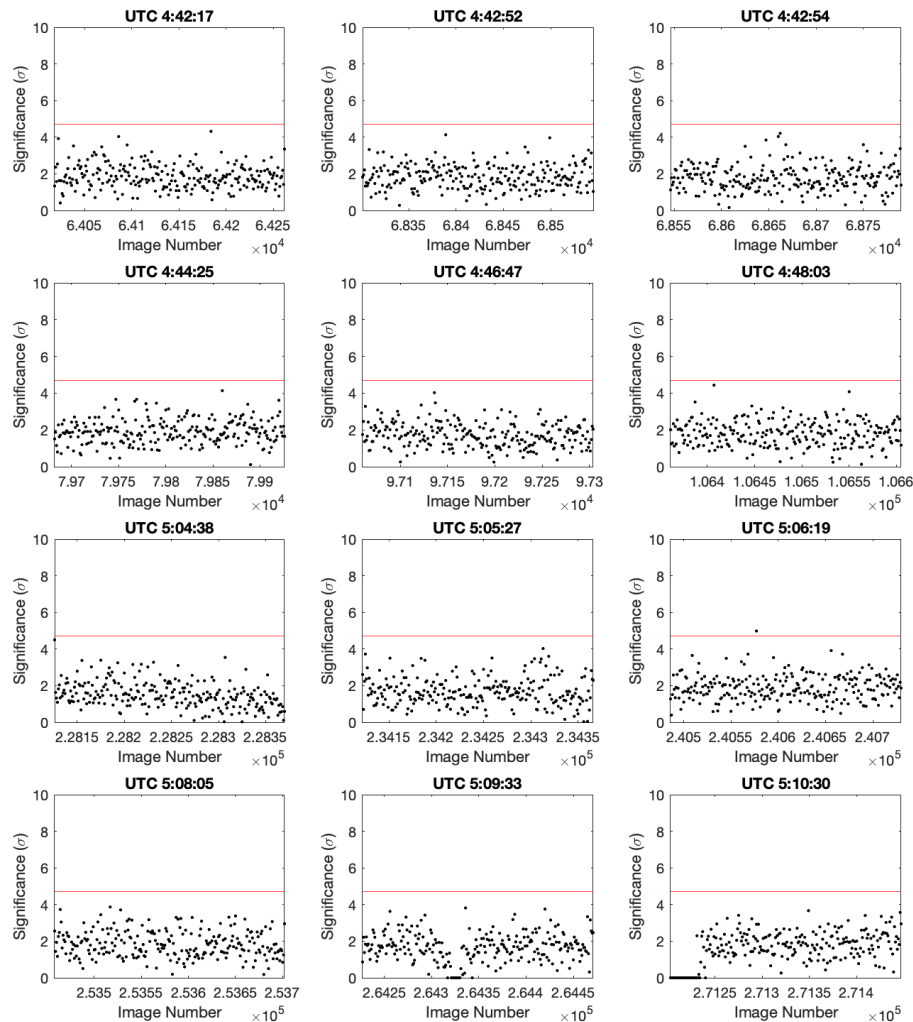


Fig. 3.13 — Detection significance versus image number for Arecibo candidate times. The red line indicates the nominal detection threshold of 4.7σ .

Only one detection, at 5:06:19 UTC, has a corresponding optical blip above the detection threshold, at 4.98σ . Figure 3.14 shows the bias-subtracted, flat-fielded, and smoothed image with the interpolated satellite position shown as a green cross. The

brightness fluctuation is offset from the satellite position by ~ 5 pixels, or $6.4''$. This is larger than image quality and uncertainty in position would account for, and the stacked image shows a very faint star trailing confirming this detection is likely a false positive.

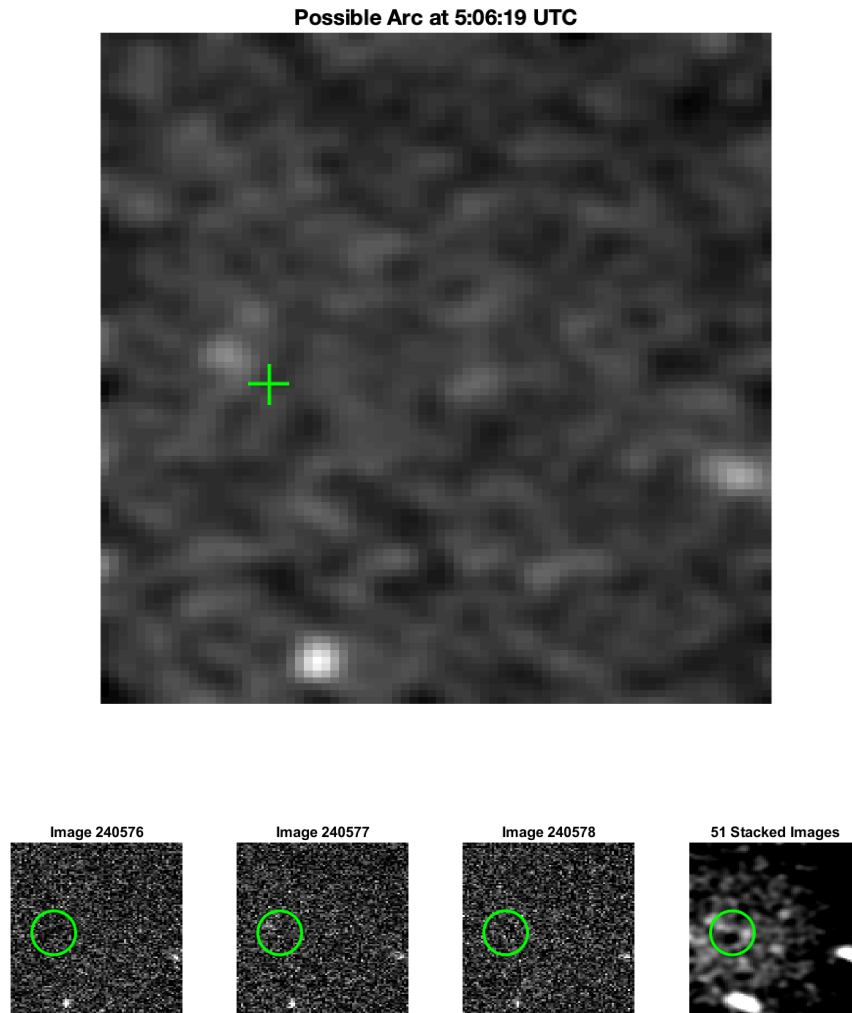


Fig. 3.14 — *Top*: Smoothed image of frame with fluctuation above threshold, corresponding to Arecibo detection at 5:06:19 UTC. Green cross is expected satellite position. *Bottom*: Image prior to detection, image of detection, image after detection, and stacked, smoothed image centered on detection showing the presence of faint stars responsible for detection. Green circle is expected satellite position.

3.6.2 NAVSTAR 59

Owing to the rotator unwrap during eclipse and failure to recover the satellite after, analysis of NAVSTAR 59 does not cover the entire eclipse period. In theory, a 360°

unwrap should put the satellite back into the same position, and its extrapolated position puts it still within the field of view. Nonetheless, it was lost and without a reliable position estimate, only pre-unwrap images can be analyzed with any confidence.

Without the benefit of independent observations to correlate candidate detections and in light of the NAVSTAR 48 results, a threshold of 5.7σ was used. This value was chosen as it was the highest false detection significance from the NAVSTAR 48 blank field. This will hold for NAVSTAR 65 as well.

Ten detections above this threshold were found: one cosmic ray, eight bright star artefacts, and one instance of the satellite shortly before umbra when illumination is not quite zero. No candidate arcs were found.

3.6.3 NAVSTAR 65

NAVSTAR 65 was observed at a lower galactic latitude, with many more stars passing through the field. It is also a Block IIF satellite, in contrast to the other two targets (IIR and IIR-M), utilizing smaller solar panels with a lower arc voltage (Ferguson et al., 2016). A fully discharging arc would therefore produce around a third of the photons than the estimate based on Block IIR from Section 1.5, just ~ 120 . Based on the transmission losses discussed in Section 3.3, even a fully discharging arc may not be visible on this satellite.

Discarding obvious stellar false positives, three detections remain. Two of these occur only 10 images (80ms) apart and the stacked images show a hint of trailing, so these are likely detections of the same star. Eliminating these, the sole remaining candidate, detected at 6.18σ occurred at 09:31:10 UTC. This detection is reasonably well centered at the expected satellite location, and the distribution of counts appears consistent with the PSF (Figure 3.15). If this is indeed an arc detection, it would correspond to 60 ± 10 detected photons (Figure 3.7), or 240 ± 40 arc photons arriving at the telescope after correcting for transmission loss. This is consistent with the expected flux from a fully discharging arc, given the many uncertainties in arriving at the expected flux. Upon examination of the stacked image, although no star trailing is obvious, it also cannot be ruled out.

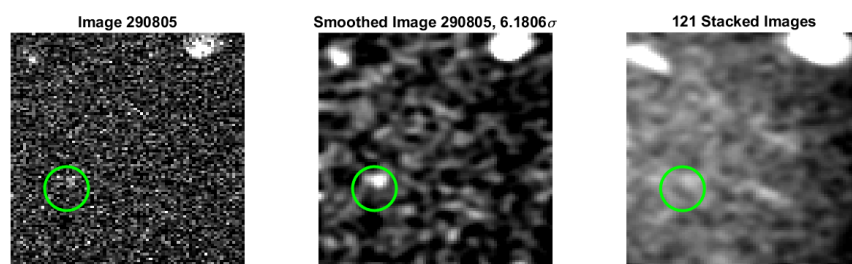


Fig. 3.15 — Candidate detection for NAVSTAR 65. *Left:* Single bias-subtracted, flat-fielded image. *Center:* Smoothed single image. *Right:* 51 Stacked and smoothed frames. Green circle shows interpolated NAVSTAR 65 location.

Chapter 4

Conclusion

You can't see me.

–John Cena

This work presents the most sensitive optical search for GPS solar panel arcs to date. The best possible result would have been a significant optical detection from NAVSTAR 48 coincident with an Arecibo detection, confirming that the radio events described in Ferguson et al. (2017) are caused by arcs. Unfortunately, despite 37 candidate detections, no optical counterparts to the Arecibo detections of NAVSTAR 48 were found. If the twelve Arecibo events during eclipse were indeed arcs, their cadence is consistent with partial discharges on the order of only $\sim 10\%$ of the maximum energy, or only ~ 36 photons arriving at the telescope. Given the high total transmission loss, these partial discharges would be undetectable.

The analysis of NAVSTAR 59 does not span the entire eclipse due the rotator unwrap and subsequent failure to recover the satellite. No candidates were detected.

NAVSTAR 65 yielded a single possible detection. If this is truly an arc detection, it corresponds to $\sim 240 \pm 40$ emitted photons, consistent with fully discharging arcs on the smaller Block II-F solar arrays. Unfortunately, it is impossible to rule out a faint star “unlucky image” as the source of this detection. Correlation with on-board telemetry would be needed to attribute this event to an arc.

With a threshold of 5.7σ and total transmission loss of 75%, the 100% detection limit is ~ 360 photons, the upper limit of expected arc brightness. The 50% detection limit is ~ 240 photons, so while no arcs were conclusively confirmed, there is motivation to repeat the experiment if transmission losses could be reduced.

4.1 Future Work

With weather only permitting one night of observations, the opportunity to learn from analysis and refine the observing strategy was denied. Without the benefit of the

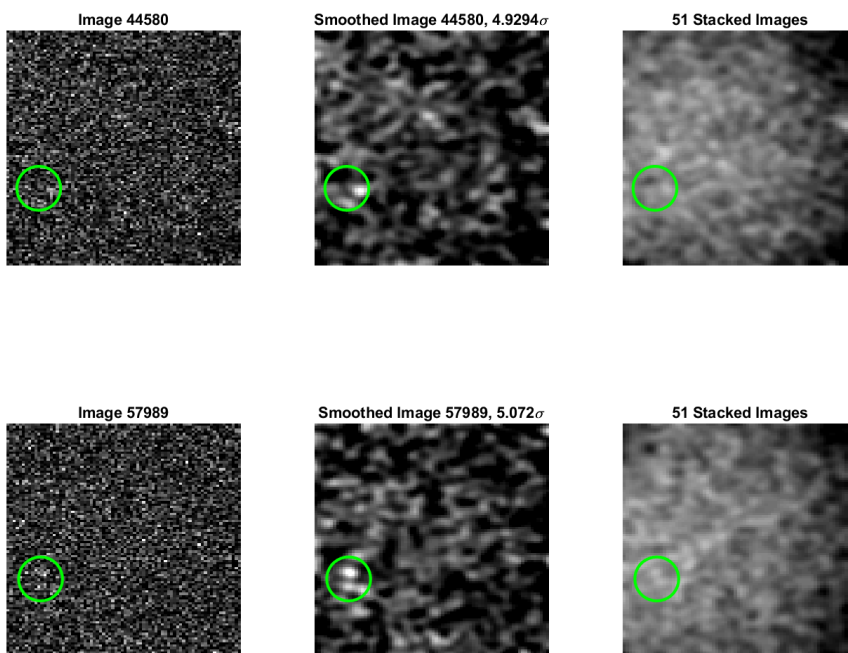
sensitivity calculation, it was not known how bright arcs could be expected to be. Having determined that they may be at the limit of sensitivity, some optimizations could be made to improve their SNR. If the wavelength distribution of arc photons was known, a filter could be used to reduce background counts while preserving the arc signal. The biggest limitation however, was the transmission losses through the system. The Red Channel provided a convenient mounting point for the EMCCD, but the extra surfaces and awkward geometry requiring the use of a relay lens wasted valuable photons. If a more direct optical path to the EMCCD could be devised, arc detection chances could improve considerably.

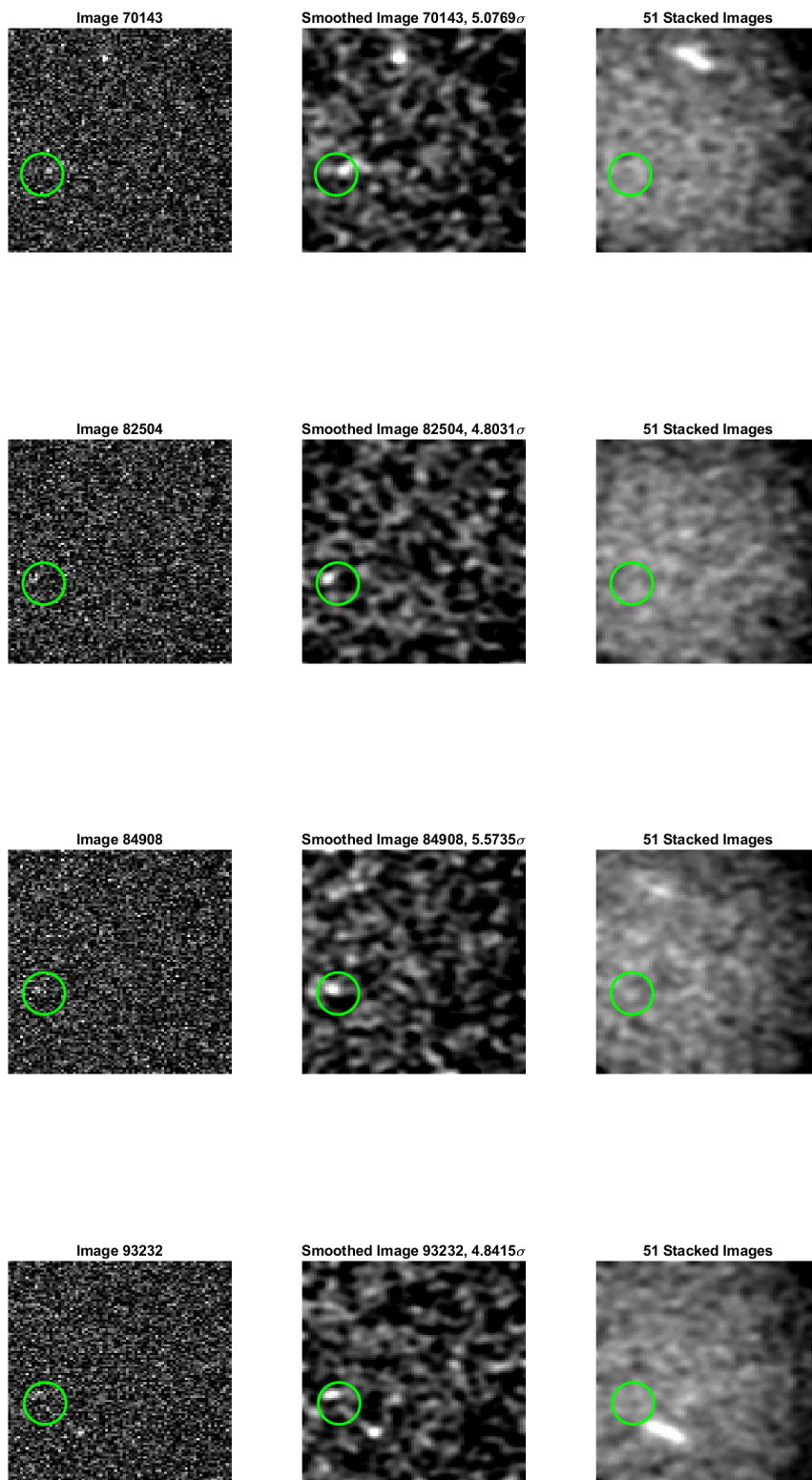
The detection algorithm used assumes that the optical energy is emitted entirely by the arc, and would be contained within a single frame. Ferguson et al. (2014) addressed the possibility of a longer duration afterglow, caused by coverglass charging and back-biasing of the solar cells. They estimated that for a satellite in GEO, the expected ground flux was $1.8 \times 10^{-18} \text{ W/m}^2$, emitted across hundreds of microseconds, although the authors acknowledged the difficulty in arriving at this estimate. Nonetheless, it is conceivable that afterglow at GPS orbit is detectable, and may span more than a single frame. Given that the brightest arcs are only at the edge of detectability, it is unlikely to have been an issue for this work but it should be considered if the experiment is repeated with improved sensitivity.

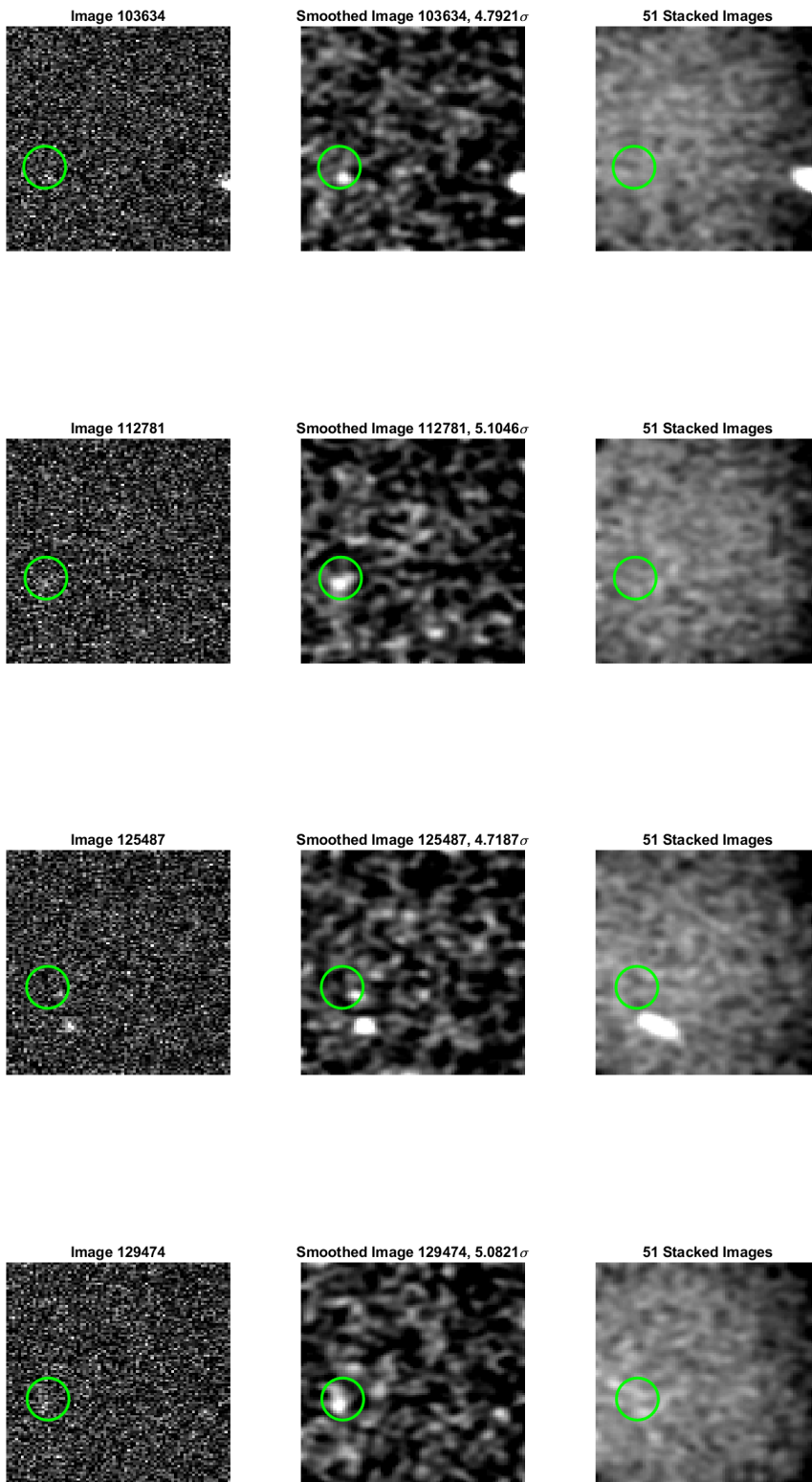
Appendix A

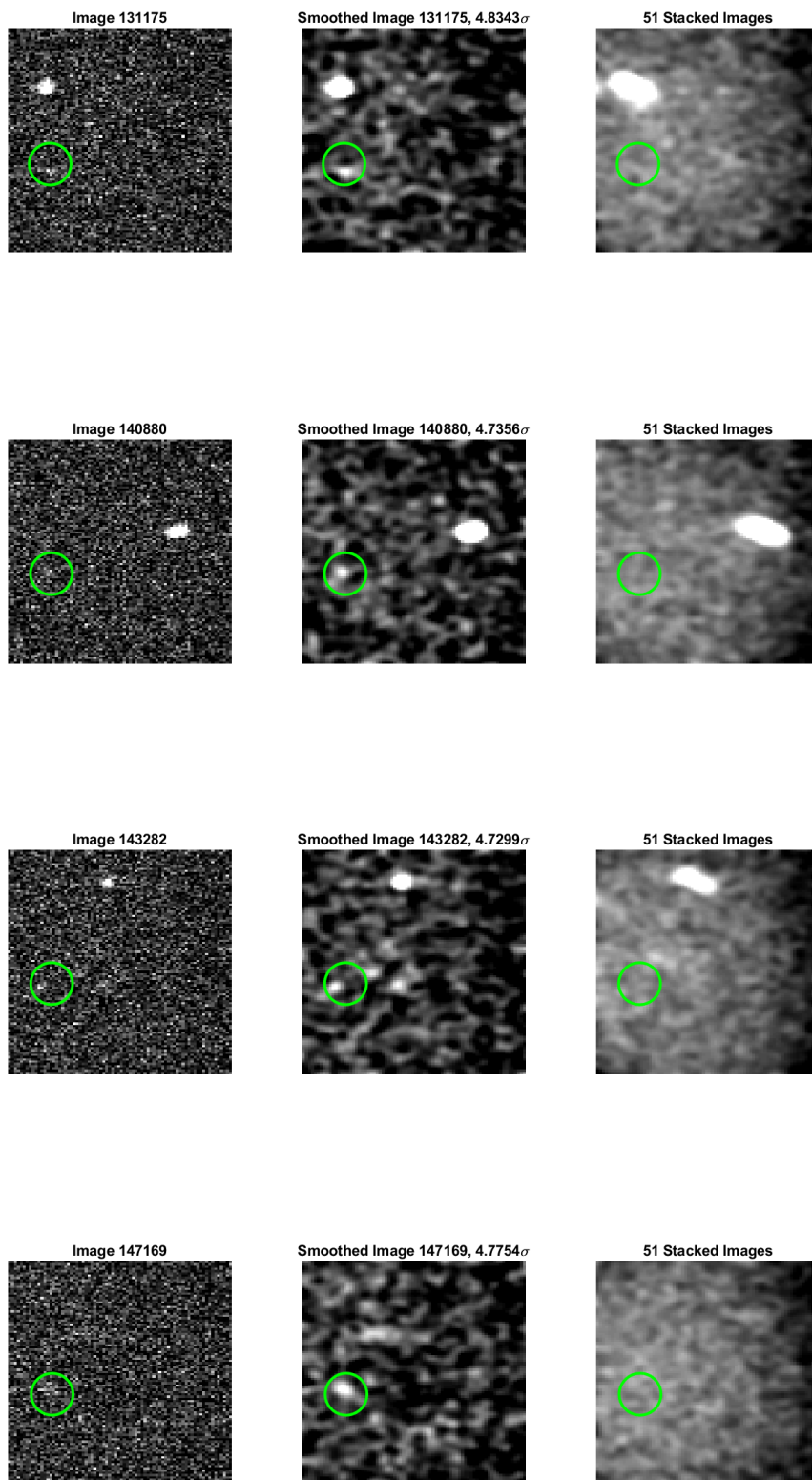
Candidate detections

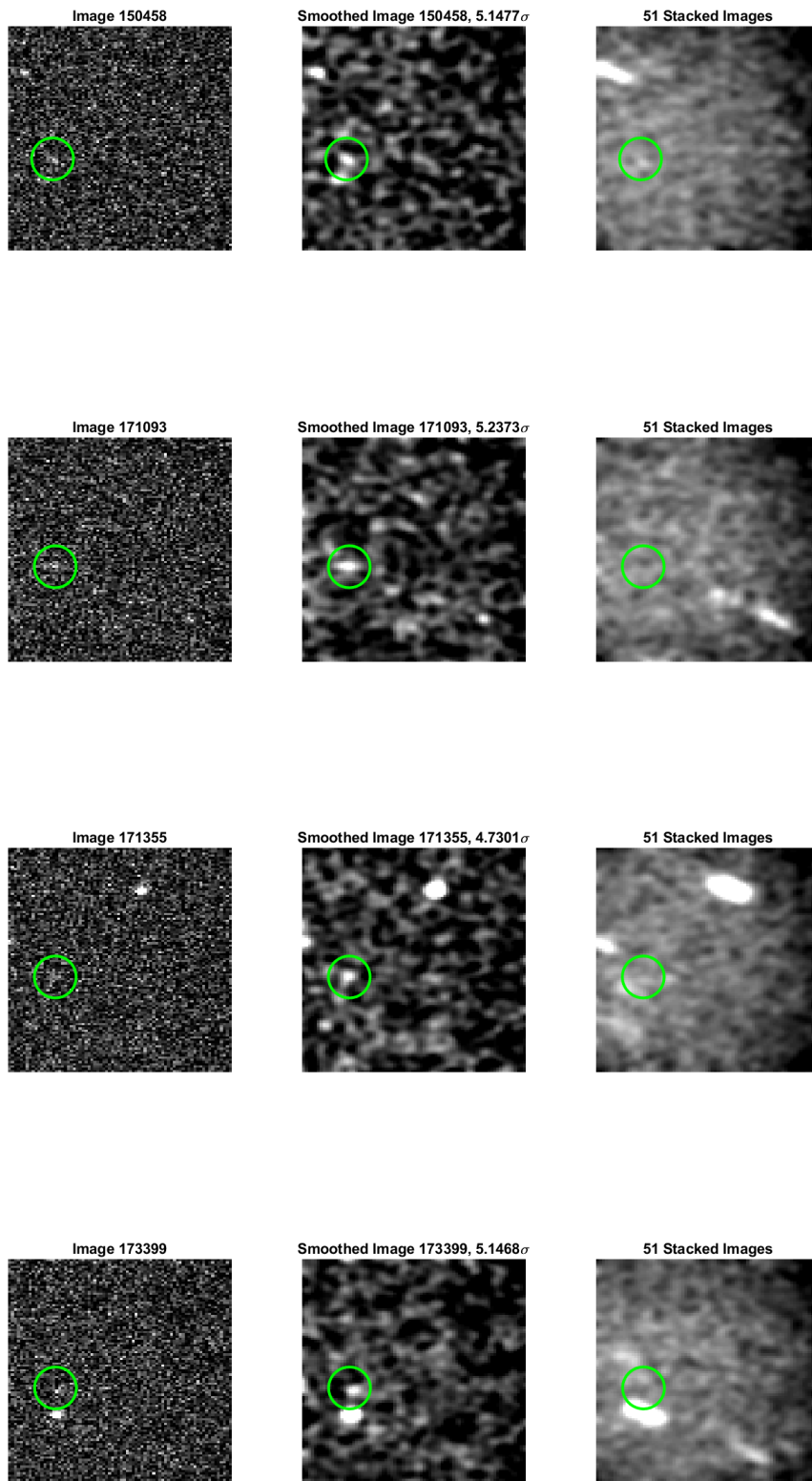
A.1 NAVSTAR 48, 4.7σ Threshold

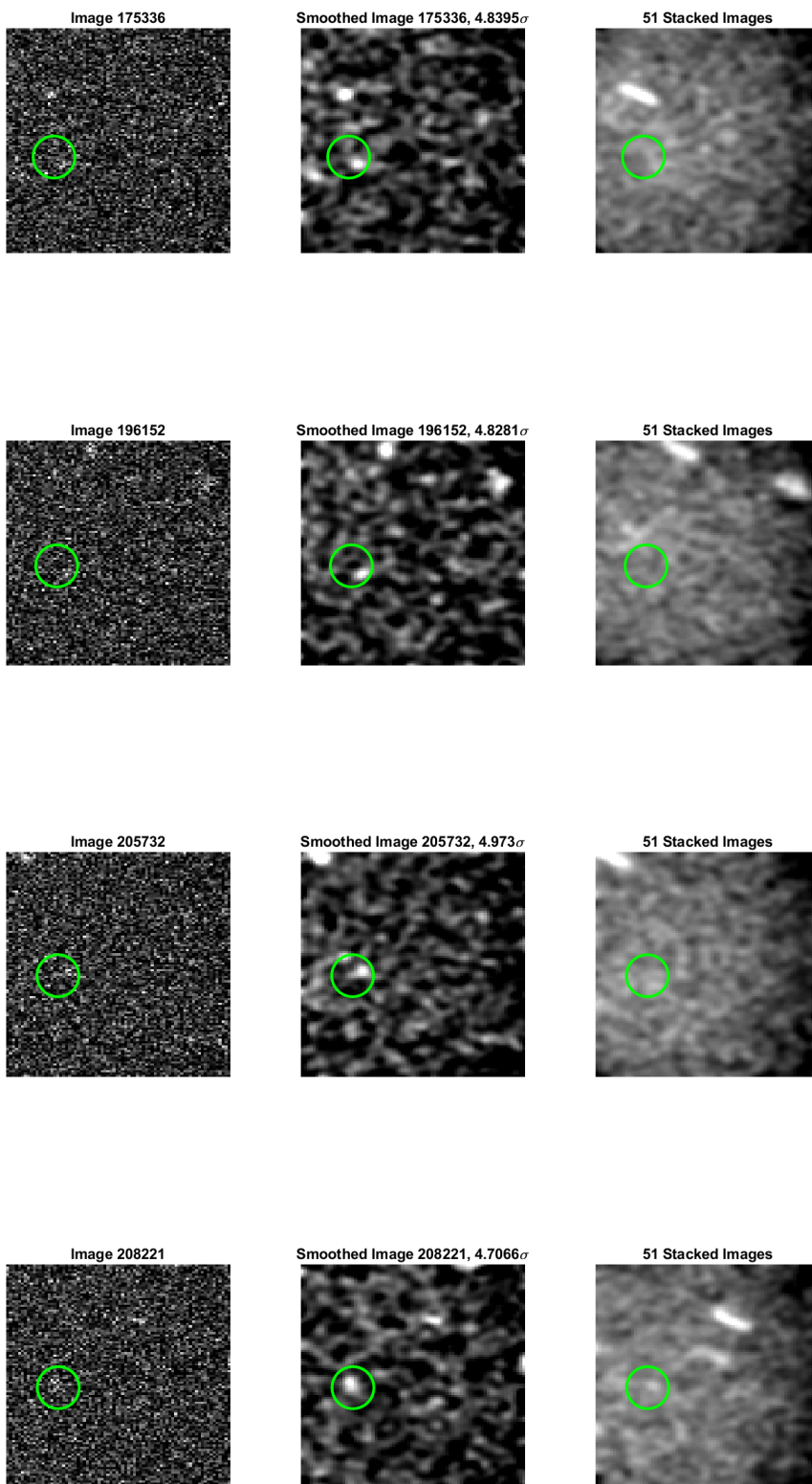


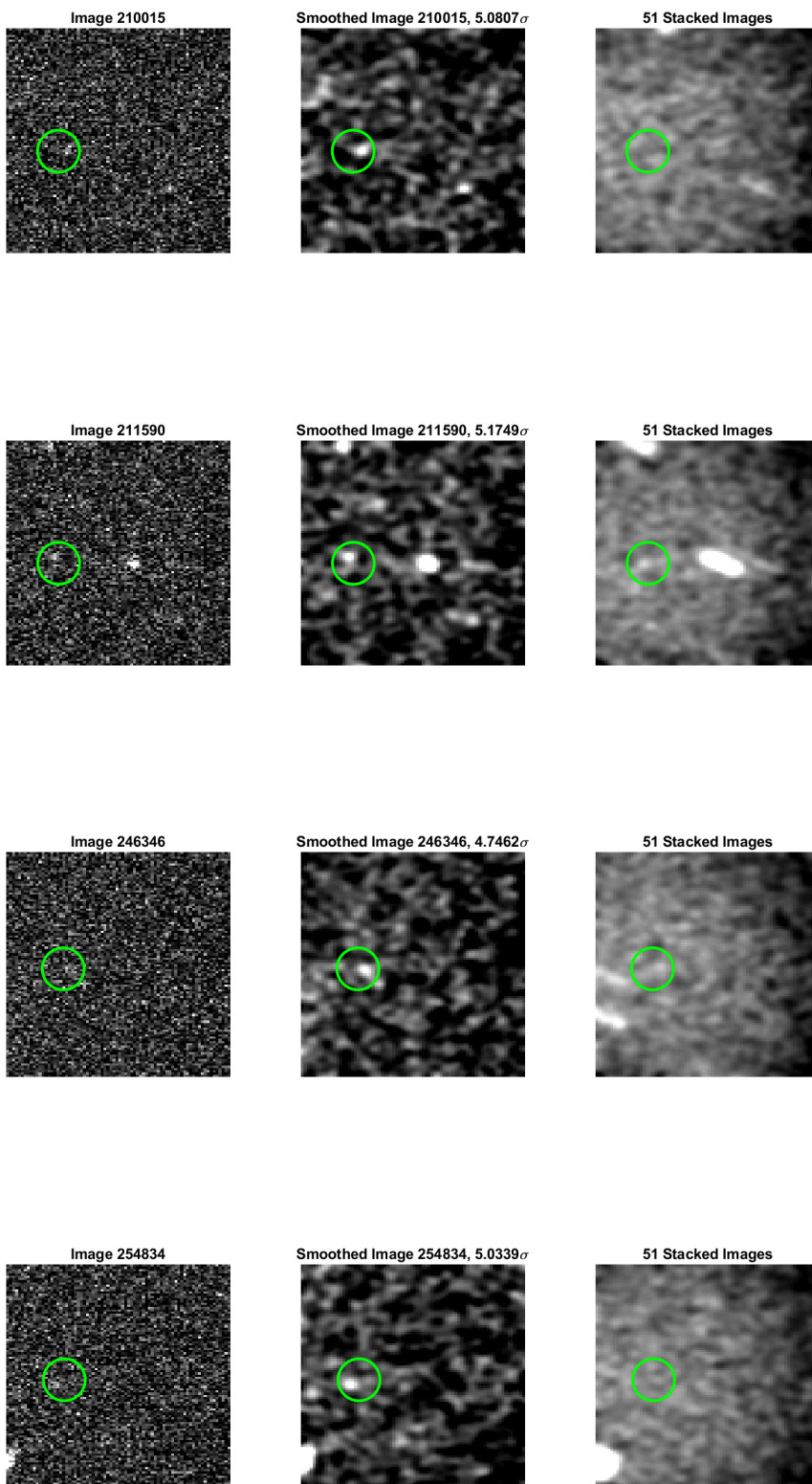


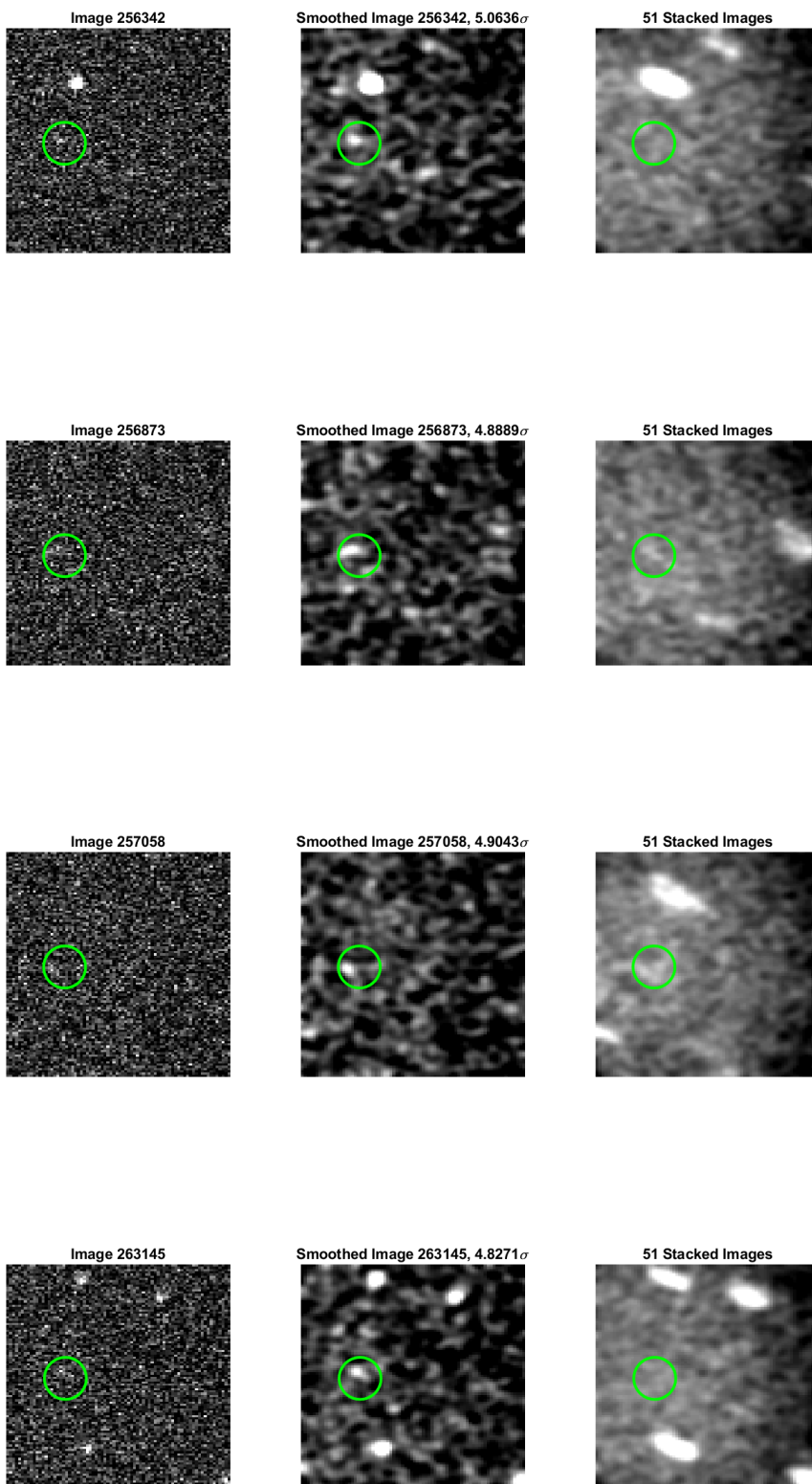












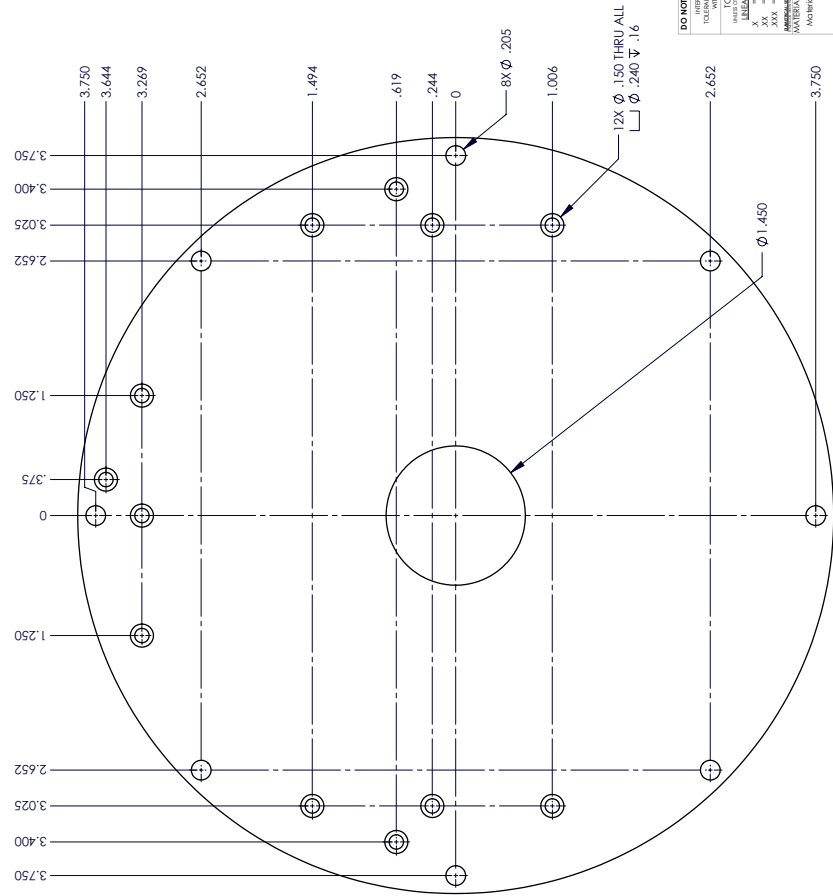
Appendix B

Mounting Bracket Engineering Drawings

| REVISION HISTORY | | | |
|------------------|-------------|------|----------|
| REV. | DESCRIPTION | DATE | APPROVED |
| 1 | PRE-RELEASE | ? | ? |

- NOTE:
1. BREAK SHARP EDGES & DEBURR.
 2. ALL MACHINING FILLETS TO BE R.015 MAX.
 3. ALL MACHINED SURFACES TO BE 125 RMS OR BETTER.

CHECK PRINT



DO NOT SCALE DRAWING THIS DRAWING CREATED IN: A3 A2 A1 A0 B1 B2 B3 B4 B5

INTERPRET DIMENSIONS & TOLERANCES WITH CARE (AS APPLICABLE)

UNIT TOLERANCES UNLESS OTHERWISE SPECIFIED:

| | |
|------------|------------|
| LENGTHS | ANGULARS |
| XXX = .01 | XXX = .01 |
| XXX = .005 | XXX = .005 |

Material not specified

FINISH

NET ASY USED ON: NET ASY USED ON: NET ASY USED ON:

ASSEMBLY APPLICATION: ASSEMBLY APPLICATION: ASSEMBLY APPLICATION:

Steward Observatory, University of Arizona

DATE: _____ PROJECT: _____ TITLE: _____

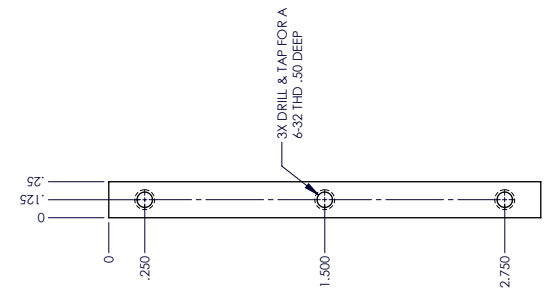
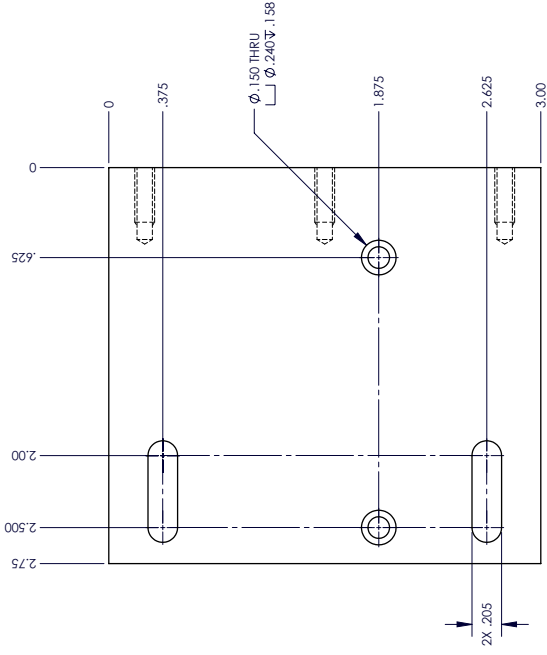
DRAWN BY: _____ CHECKED BY: _____

DESIGNED BY: _____

DRAWING NUMBER: _____ SHEET 1 OF 1

REV: _____

| REVISION HISTORY | | | |
|------------------|-------------|------|-------------|
| REV. | DESCRIPTION | DATE | APPROVED BY |
| 1 | PRE-RELEASE | ? | ? |



CHECK PRINT

- NOTE:
1. BREAK SHARP EDGES & DEBURR.
 2. ALL MACHINING FILLETS TO BE R.015 MAX.
 3. ALL MACHINED SURFACES TO BE 125 RMS OR BETTER.

DO NOT SCALE DRAWING THIS DRAWING CREATED IN: ACAD PLOT DWT DWG

INTERPRET DIMENSIONS & TOLERANCES TO ACCORDANCE WITH ASME Y14.5M

TOLERANCES UNLESS OTHERWISE SPECIFIED: ANGULAR ±1°
 HOLE DIA ±.01
 XXX ±.005
 MATERIAL: 6061-T6 ALUMINUM
 MATERIAL AND SPECIES: Material and species

FINISH

NEXT ASY USED ON:

ASSEMBLY APPLICATION:

DATE:

PROJECT:

TITLE:

DRAWN BY:

CHECKED BY:

DATE APPROVED:

DESIGNED BY:

DATE DESIGNED:

PROJECT NUMBER:

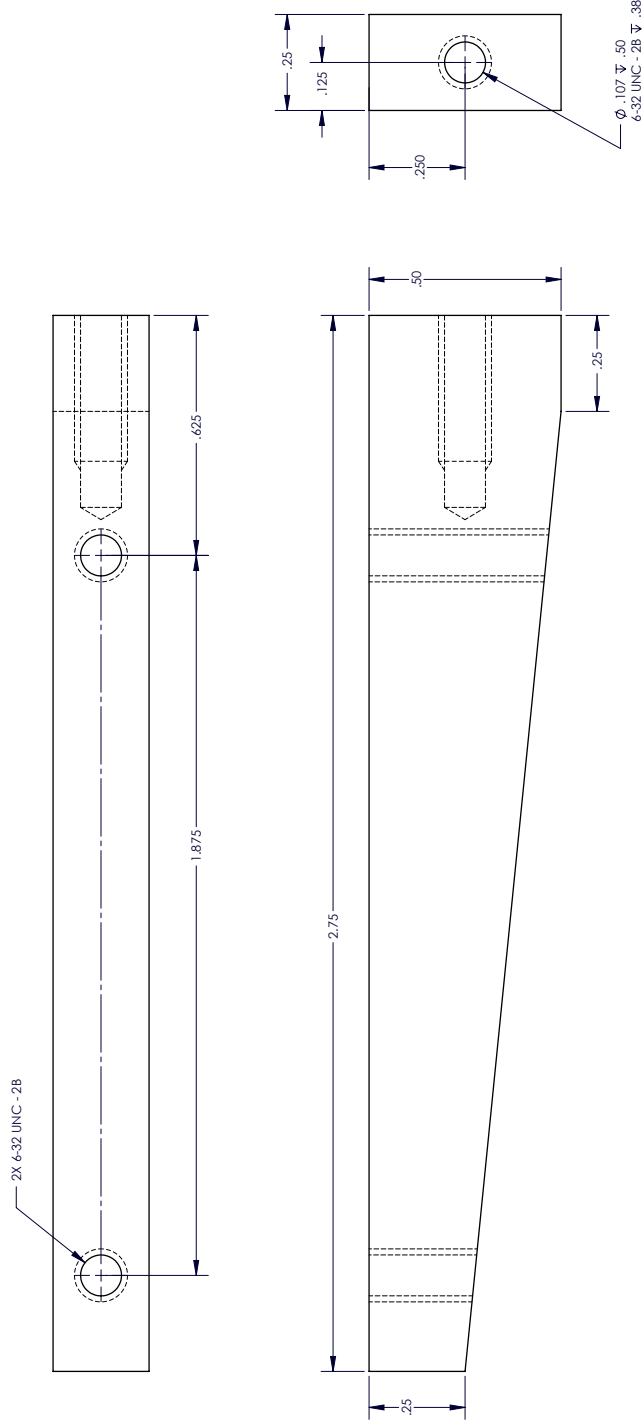
DRAWING NUMBER:

SHEET 1 OF 1

REV

Steward Observatory, University of Arizona

| REVISION HISTORY | | | |
|------------------|-------------|------|-------------|
| REV. | DESCRIPTION | DATE | APPROVED BY |
| 1 | PRE-RELEASE | ? | ? |



| | | | |
|---|---------|--------------------------|----|
| DO NOT SCALE DRAWING | | THIS DRAWING CREATED IN: | |
| ACAD | INCH | DATE | BY |
| INTERPRET DRAWINGS & DIMENSIONS TO ACCORDANCE WITH ASME Y14.5M-2018 | | | |
| TOLERANCES UNLESS OTHERWISE SPECIFIED: | | FORMER | |
| LINEAR | ANGULAR | DESIGNER | |
| XX ± .01 | ± 1° | DRAWER | |
| XXX ± .005 | | CHECKER | |
| SURFACE FINISH UNLESS OTHERWISE SPECIFIED: | | IN CHARGE | |
| Material and specification | | DESIGNED BY | |
| FINISH | | USED ON | |
| | | DESIGNED BY | |
| | | ASSEMBLY APPLICATION | |

Steward Observatory, University of Arizona
1500 E. SAUNDERS AVENUE, TUCSON, AZ 85724-5160 (520) 971-7600

CHECK PRINT

NOTE:

- BREAK SHARP EDGES & DEBURR.
- ALL MACHINING FILLETS TO BE R.015 MAX.
- ALL MACHINED SURFACES TO BE 125 RMS OR BETTER.

| | | |
|-----------------|----------|--------|
| DATE: | PROJECT: | TITLE: |
| CATEGORY: | | |
| DRAWING NUMBER: | | |
| SHEET 1 OF 1 | | |

Appendix C

MATLAB Code

C.1 spade_search.m

This is the main code that cycles through the images of the chosen satellite and outputs a FITS file with the maximum value within the detection box of the final masked image for every image.

```
close all
clearvars

% Choose satellite
images = dir("D:\MMI\GPS\26407*");
%images = dir("D:\MMI\GPS\29601*");
%images = dir("D:\MMI\GPS\36585*");
total_images = size(images,1);

image_start = 1;
image_end = total_images;

good_images = image_end-image_start+1;

flat = fitsread("superflat.fits");
threshold = 4.7;

edge_mask = zeros(100,76);
edge_mask(6:95,6:71) = 1;
stack = zeros(100,76,5);
maximums = [];
imgnums = [];

% Analyze images
for n = image_start+2:5:image_end-2
    round((n-image_start)/good_images*100,2) % Show progress
```

```

% Read 5 consecutive images into a cube
data1_r = fitsread(images(n-2).folder+"/"+images(n-2).name);
data1_r = data1_r(16:115,16:91)-624;
data1_r = data1_r./flat;
data1_r = imgaussfilt(data1_r,1.5);

data2_r = fitsread(images(n-1).folder+"/"+images(n-1).name);
data2_r = data2_r(16:115,16:91)-624;
data2_r = data2_r./flat;
data2_r = imgaussfilt(data2_r,1.5);

data3_r = fitsread(images(n).folder+"/"+images(n).name);
data3_r = data3_r(16:115,16:91)-624;
data3_r = data3_r./flat;
data3_r = imgaussfilt(data3_r,1.5);

data4_r = fitsread(images(n+1).folder+"/"+images(n+1).name);
data4_r = data4_r(16:115,16:91)-624;
data4_r = data4_r./flat;
data4_r = imgaussfilt(data4_r,1.5);

data5_r = fitsread(images(n+2).folder+"/"+images(n+2).name);
data5_r = data5_r(16:115,16:91)-624;
data5_r = data5_r./flat;
data5_r = imgaussfilt(data5_r,1.5);

stack(:,:,1) = data1_r;
stack(:,:,2) = data2_r;
stack(:,:,3) = data3_r;
stack(:,:,4) = data4_r;
stack(:,:,5) = data5_r;

stack_flat = median(stack,3); % flatten stack by median across frames
stack_flat_stats = rmoutliers(stack_flat(:),'percentiles',[0 90]);
stack_median = median(stack_flat_stats);
stack_std = std(stack_flat_stats);
stack_mask =(stack_flat-stack_median)/stack_std < 5;

% Run a moving minimum to expand the masked regions
stack_mask = movmin(stack_mask,5,1);
stack_mask = movmin(stack_mask,5,2);

for k = 1:5
    imgnum = n-3+k;

    % Uncomment desired satellite
    % Blank field
    %x_expected = 65;

```

```

%y_expected = 40;

% Satellite 36585
%x_expected = -37/total_images*imgnum+46
%y_expected = 38/total_images*imgnum+39

% Satellite 26407
x_expected = 14/total_images*imgnum+25-16
y_expected = -24/total_images*imgnum+87-16

% 29601
%x_expected = -0.000016666851854*imgnum+58-16
%y_expected = 0.000066667407416*imgnum+71-16

xlow = round(x_expected - 4);
ylo = round(y_expected - 4);

current_image = stack(:, :, k);
image_med = median(current_image(stack_mask ==1));
image_std = std(current_image(stack_mask ==1));
scaled_image = (current_image-image_med)/image_std;
masked_image = scaled_image.*stack_mask.*edge_mask;

maxvalue = max(masked_image(ylo:ylo+8,xlo:xlo+8), [], 'all')
maximums = [maximums, maxvalue];
imgnums = [imgnums, imgnum];
% Show a plot for any detections
if maxvalue > threshold

    figure
    set(gcf, 'Position', [100, 100, 250, 1000])
    subplot(4,1,1)
    imagesc(masked_image)
    colormap(gray)
    hold on
    axis square
    axis off
    imgnum = string(n-3+k)
    title("Central Image #" +imgnum)
    xlabel("Max Val =" +maxvalue+"\sigma")

    subplot(4,1,2)
    previous = fitsread(images(n-3+k-1).folder + "/" +images(n-3+k-1)
        .name);
    imagesc(previous(16:115,16:91), [600 1200])
    colormap(gray)
    hold on
    axis square

```

```

axis off

subplot(4,1,3)
current = fitsread(images(n-3+k).folder+"/")+images(n-3+k).name
);
imagesc(current(16:115,16:91),[600 1200])
colormap(gray)
hold on
axis square
axis off

subplot(4,1,4)
next = fitsread(images(n-3+k+1).folder+"/")+images(n-3+k+1).
name);
imagesc(next(16:115,16:91),[600 1200])
colormap(gray)
hold on
axis square
axis off
end

end

end

% Write maximum values to file for later analysis
fitswrite(maximums,"maximums_29601.fits")

```

C.2 spade_monte.m

The code for the Monte Carlo simulation for estimating detection efficiency and optimum threshold.

```

close all
clearvars

n_photonset = linspace(0,120,21);

% Number of iterations per photon value
m=1000;
counts = zeros(m, size(n_photonset,2));
skycounts = zeros(m, size(n_photonset,2));
detected = zeros(m, size(n_photonset,2));
skymean = 303;
skysigma = 96;

threshold = 5.7;
figure

```

```

for k = 1:size(n_photonset,2)
n_photons = n_photonset(k)
for n = 1:m
    n;
    data1 = randn(100,76)*skysigma + skymean;

    % Add some random jitter to arc center to mix things up.
    x_expected = randn(1)*0.83+35;
    y_expected = randn(1)*0.83+47;
    data1 = arcmaker(data1,n_photons,x_expected,y_expected);
    fakearcs(n,k) = 1;

    data1 = imgaussfilt(data1,1.5);
    data1vect = data1(:);
    clipmed = median(rmoutliers(data1vect,'percentiles',[0 99]));
    clipsig = std(rmoutliers(data1vect,'percentiles',[0 99]));
    data1 = (data1-clipmed)/clipsig;

    xlow = round(x_expected - 4);
    ylow = round(y_expected - 4);
    databox = data1(ylow:ylow+8,xlow:xlow+8);
    skybox = data1(ylow+20:ylow+8+20,xlow+20:xlow+8+20);
    counts_current = max(databox(:));
    sky_current = max(skybox(:));
    counts(n,k) = counts_current;
    skycounts(n,k) = sky_current;
    detected(n,k) = counts_current > threshold;
    false_detected(n,k) = sky_current > threshold;
end
subplot(7,3,k)
imagesc(data1,[-2 5])
colormap(gray)
axis square
axis off
end

figure
imagesc(counts)
det_eff = sum(detected,1)/m*100;
false_pos = sum(false_detected,1)
n_samples = m*size(n_photonset,2)
plot(n_photonset,det_eff,'-k');
hold on
plot(n_photonset,det_eff,'.k','MarkerSize',10)
title("Detection Efficiency vs Number of Arc Photons")
xlabel("Detected Arc Photons (n)")
ylabel("Detection Efficiency (%)")

```

```

figure
meanmax = mean(counts,1);
stdcounts = std(counts,1);
maxsky = max(skycounts,[],1);
meansky = mean(skycounts,1);
stdsky = std(skycounts,1);
plot(n_photonset,meanmax,'-r','LineWidth',2)
hold on
plot(n_photonset,meansky,'-b','LineWidth',2)
plot(n_photonset,meansky+4.5*stdsky,'--b','LineWidth',1)
plot(n_photonset,meanmax+3*stdcounts,'--r','LineWidth',1)
plot(n_photonset,meanmax-3*stdcounts,'--r','LineWidth',1)
plot(n_photonset,meanmax+1*stdcounts,'-r','LineWidth',1)
plot(n_photonset,meanmax-1*stdcounts,'-r','LineWidth',1)
ylim([0 15])

title("Average Significance vs Number of Arc Photons")
xlabel("Detected Arc Photons (n)")
ylabel("Average Significance (\sigma)")
legend("Arcs","Background","location","northwest")
fitswrite(maximums,"maximums_29601.fits")

```

C.3 arcmaker.m

Function that takes an input image and adds an arc of the specified number of photons at the specified position, and returns the new image.

```

function arc_image = arcmaker(image,n_photons,x,y)
x_size = size(image,2);
y_size = size(image,1);
EMgain = 100;
gain = 3;
n_counts = round(n_photons*EMgain/gain);

arc_x = randn(n_counts,1)*0.83+x;
arc_y = randn(n_counts,1)*0.83+y;
X = [arc_y,arc_x];

arc = hist3(X,'ctrs',{1:1:y_size 1:1:x_size},'CdataMode','auto');
arc_image = arc + image;
end

```

Bibliography

- C. Jordan, D., & R. Kurtz, S. 2013, Progress in Photovoltaics: Research and Applications, 21
- Ferguson, D., Crabtree, P., White, S., & Vayner, B. 2016, Journal of Spacecraft and Rockets, 53, 464
- Ferguson, D., White, S., Rast, R., Balasubramaniam, K., Thompson, D., Suszcynsky, D., & Holeman, E. 2017, Journal of Spacecraft and Rockets, 54, 566
- Ferguson, D. C., Murray-Krezan, J., Barton, D. A., Dennison, J. R., & Gregory, S. A. 2014, Journal of Spacecraft and Rockets, 51, 1907
- Kucerovsky, Z., Greason, W., & Flatley, M. 2002, Industry Applications, IEEE Transactions on, 38, 77
- Marvin, D., Hwang, W., & Simburger, E. 1988, Conference Record of the Twentieth IEEE Photovoltaic Specialists Conference
- Massey, P., & Foltz, C. B. 2000, PASP, 112, 566
- Massey, P., Strobel, K., Barnes, J. V., & Anderson, E. 1988, ApJ, 328, 315
- Messenger, S. R., Jackson, E. M., Warner, J. H., Walters, R. J., Cayton, T. E., Chen, Y., Friedel, R. W., Kippen, R. M., & Reed, B. 2011, IEEE Transactions on Nuclear Science, 58, 3118
- Pedani, M. 2009, PASP, 121, 778
- Schmidt, G. D., Weymann, R. J., & Foltz, C. B. 1989, PASP, 101, 713
- Tribble, A. C., & Haffner, J. W. 1991, Journal of Spacecraft and Rockets, 28, 222